Damage characterization of CFRP laminates using acoustic emission and digital image correlation: Clustering, damage identification and classification

Lala Bahadur Andraju, Gangadharan Raju *

Department of Mechanical and Aerospace Engineering, Indian Institute of Technology Hyderabad, India

ARTICLE INFO

ABSTRACT

Damage mechanisms in composite laminates are quite complex, and it is necessary to perceive their effects on the degradation of laminate mechanical properties. This work employs acoustic emission (AE) and digital image correlation (DIC) techniques to describe the evolution of intra/inter-laminar damage modes in the CFRP laminates under in-plane/out-of-plane loading conditions. In this study, laminates of stacking sequences $[90^0]_8$, $[45^0]_8$, $[45^0/-45^0]_{2s}$, and $[0^0]_8$ under tensile load are investigated to distinguish the intra-laminar damages like matrix cracking, fiber–matrix debond, and fiber breakage. Double cantilever beam, end notch flexure, and mixed-mode bending specimens are used to characterize delamination failure in the laminate. An unsupervised k-means clustering technique is used to classify the AE data based on peak frequency and amplitude. The surface displacement and strain data are evaluated using the DIC technique to understand the damage evolution in the laminates. Post failure analysis is carried out using a digital microscope, and fractography studies are used to identify and assign the damages to different AE clusters. This investigation yields a taxonomy of damage modes, their sequence of occurrence, and failure strains that can be used for structural health monitoring and progressive damage modeling of composite laminates.

1. Introduction

Cognizance of the various damage modes like fiber failure, matrix cracking, delamination, and their progression leading to failure mechanisms are essential for damage tolerant design of composite structures. The damage evolution in composite laminate influences the elastic stiffness properties, which in turn leads to a nonlinear constitutive relationship governing the mechanical behavior of the laminate. The quantification of damage information using the available experimental techniques is essential for the development of progressive damage models at multiple spatial scales of the laminate. Various non-destructive evaluation (NDE) techniques are used to identify and characterize the damage modes in composites. Acoustic emission is one such NDE technique that is widely used to detect and classify the damage modes in real-time by analyzing the transient waves generated by crack propagation in the laminate [1–3]. When an array of AE sensors are used, the damage location in the laminate can be accurately determined if the velocities of the propagating elastic wave modes are known [4–8]. Another technique that is widely used for damage characterization of laminates is digital image correlation (DIC). It is a non-contact optical measurement technique that monitors the surface displacement/strain field evolution of the laminate with the applied load [8,9]. In this work, the experimental results from AE and DIC techniques are combined together to understand the damage evolution in composite laminates.

* Correspondence to: Department of Mechanical and Aerospace Engineering, IIT Hyderabad, Kandi, Sangareddy, Telangana, 502285, India.
E-mail addresses: lalbahadur.andraju@gmail.com (L.B. Andraju), gangadharanr@mae.iith.ac.in (G. Raju).

Numerous works have been reported on classifying AE signals based on the damages like matrix cracking, fiber failure, delamination, etc., which helps in real-time structural health monitoring (SHM) applications. Many researchers have studied specimens under in-plane and out-of-plane loading to categorize damage modes in laminated composites using various AE parameters [10]. Open hole tension (OHT) [11–15] and compression tests [16–18] were carried out to characterize various damages and their interactions leading to final failure in composite laminate using AE. Also, the AE technique is used to identify damage modes under out-of-plane loading like indentation and low-velocity impact [19,20]. Andraju et al. [21,22] used the AE technique to differentiate damage modes and their sequence in the CFRP laminate under flexural loading. Further, AE technique was used to characterize damage modes in the adhesive bonded composite laminates [23,24].

Prior knowledge of the AE features related to individual damage may help in characterizing the damage modes in composite laminate under various loading conditions. Giordano et al. [25] carried out a single fiber test under tension to characterize the fiber breakage using various AE parameters. Huguet et al. [26] carried out tensile tests on pure resin and composite laminate specimens (45^0 and 90^0 off-axis unidirectional samples) and used Kohonen's map to cluster the AE signals to differentiate various damages. Ech et al. [27] developed an incremental clustering method to classify different damages in specimens of epoxy and composite laminates with different orientations, and the results were verified with the k-means clustering technique. Delamination is characterized using AE parameters based on double cantilever beam (DCB) [28–30], end notch flexure (ENF) [31], and mixed-mode bending (MMB) tests [32–34].

Various AE parameters are extracted from the waveform [35] for damage classification, but it is challenging to select the appropriate ones to differentiate damage modes in composite laminates. Among all the AE parameters, amplitude and peak frequency are the most commonly used to cluster AE data [13,14,20,36–38]. Also, other parameters like duration [39–41], rise time [40,42], frequency centroid [24,43] etc., have been used to cluster the AE events. In addition, Barile et al. [44] used the Lempel-Ziv (LZ) complexity [45] to identifying different damage modes in CFRP laminates at elevated temperature. Studies have shown that selection of few AE parameters helps in reducing the dimension of data used for clustering and assists in better damage classification. Pearson correlation coefficients [14], principal component analyses [38], Laplacian score [24,46], spectral feature selection method, and multi-cluster feature selection method [47] are some of the traditional approaches used for clustering of AE data.

Recently, various machine learning algorithms have been applied to analyze AE data to classify the damage modes in composite laminates. Ozaslan et al. [14] used k-means clustering algorithm to classify various damage in CFRP composite laminate in OHT specimens, and the AE results are complemented with DIC measurements. Xu et al. [48] used the k-means++ clustering technique to identify different damage modes in single lap joint laminate subjected to hygrothermal aging. Godin et al. [49] used a combined k-means and k-nearest neighbor techniques to cluster the damages in GFRP composite laminate under tensile load. Sause et al. [50] proposed an AE based approach using an artificial neural network (ANN) to predict the failure load under tension. McCrory et al. [51] used ANN analysis, unsupervised waveform clustering and corrected measured amplitude ratio techniques to locate and classify the type of damage modes occurring in a buckled CFRP panel. Saeedifar et al. [20] used various clustering techniques like k-means, genetic k-means, fuzzy C-Means, Self-Organizing Map (SOM), Gaussian Mixture Model (GMM), and hierarchical model to classify damages in quasi-isotropic laminates under indentation load. Bhat et al. [52] used ANN to remove the noise in the AE signals and characterized the failures in the CFRP laminate under fatigue load. The main challenge in the clustering techniques is to select the optimum number of clusters to classify the damage. Barile et al. [53] used AE spectrograms to train the Convolution Neural Network (CNN), and then used for monitoring the delamination propagation in DCB specimen. Various indices are available to select the optimum number of clusters for the given data set. Examples are Silhouette index [54], Calinski–Harabasz Index [55], Davies–Bouldin Index [38,56], Gap Statistic [57], Elbow Method [58] etc,. These parameters are evaluated based on the given data set, but they do not provide any damage information of the cluster.

Furthermore, employing AE alone may not be good enough to classify damages in the composite laminate under different loading conditions. So it is better to combine AE with complementary experimental techniques to identify different damage modes in composite laminates more precisely. Maillet et al. [59] combined acousto-ultrasonics and AE techniques for real-time damage monitoring in SiC/SiC minicomposites. In addition to AE, DIC technique is used by various researches to be cognizant of failure modes in composite laminates [14,21,22,60–62]. Munoz et al. [63] coupled AE and infrared thermography to identify damages in CFRP laminates under tensile load.

In this work, a unified approach is developed using AE, DIC, and fractography to characterize the intra/inter-laminar damage modes in CFRP laminates. In literature, a specimen of specific stacking sequence is mainly studied to cluster and classify the AE data. This information may not be sufficient to create a sophisticated tool for structural health monitoring of composites under different loading conditions. Additional information, such as the failure strain of various damage modes, are required to develop physics based damage models, which are helpful in the SHM of composite structures. The current study addresses the issue by considering specimens with different stacking sequences under in-plane/out-of-plane loading conditions. The laminates are chosen in such a way that the damage is limited to one or two modes which can give more coherence on the individual damages based on the AE and DIC data, which assist in their classification as well as provide failure strain information. The intra-laminar damages are studied by tensile testing of laminates with different orientations under quasi-static loading, whereas the inter-laminar failure like delamination is investigated using standard mode-I, mode-II, and mixed-mode testing. The experimental AE data are analyzed, and various AE parameters are used to differentiate the damage modes in composite laminate at the coupon level. An unsupervised k-means clustering algorithm is used to cluster the AE events. Later, the DIC displacement and strain data evolution with damage is investigated to extract the failure strain of damage modes, and fractography studies are carried out to identify different damage modes in the laminates. Further, DIC and fractography results are used to assign AE clusters to different damage modes in the laminates. The combined AE and DIC results provide insights into the development of damage models for studying failure in composite laminates.

Table 1

Stacking sequence and dimensions of CFRP laminate tensile test specimens for intra-laminar damage characterization.

Name	Stacking sequence	Gauge length	Laminate thickness	Width
UD90	$[90^0]_8$	100 mm	1.6 mm	20 mm
UD45	$[45^0]_8$	100 mm	1.6 mm	20 mm
Q±45	$[45^0/-45^0]_{2s}$	100 mm	1.6 mm	20 mm
UD0	$[0^0]_8$	100 mm	1.6 mm	20 mm

Table 2

CFRP laminates with initial delamination to characterize the mode-I, mode-II, and mixed-mode delamination.

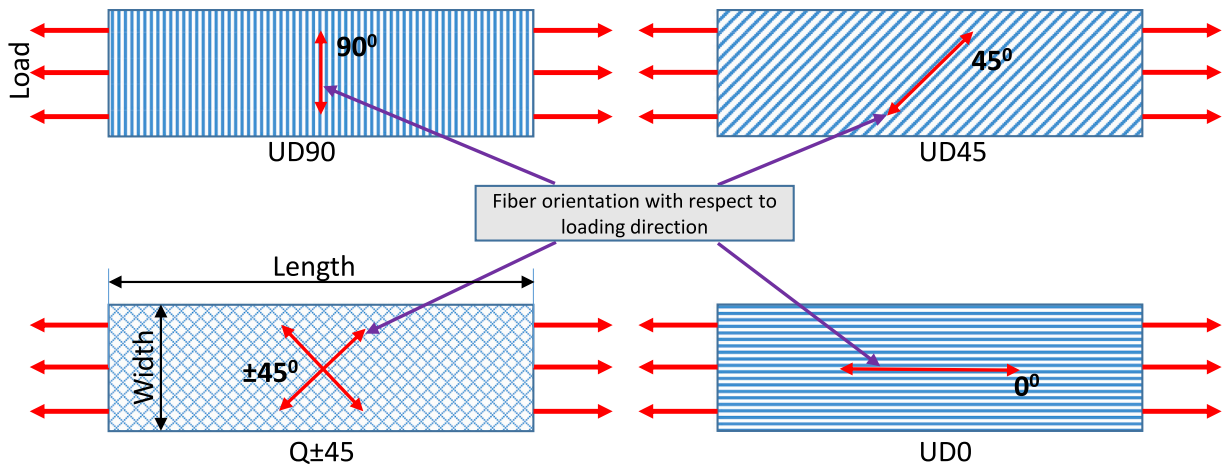| Name	Length	Width	Thickness	Initial crack length (a)
Double cantilever beam (DCB)	150 mm	25 mm	4 mm	50 mm
End notch flexure (ENF)	205 mm	30 mm	4 mm	50 mm
Mixed mode bending (MMB)	150 mm	25 mm	4 mm	35 mm

Fig. 1. Schematic of the tensile test specimens considered to characterize intra-laminar damage and the fiber orientation with respect to the loading direction.

2. Experimental studies

2.1. Materials and fabrication procedure

The CFRP laminates are fabricated in-house using hand layup and vacuum bagging technique. The uni-directional carbon dry fabric (HinFab® Uni-directional fabric) of 200 GSM supplied by Hindoostan composite solutions limited is used for the laminate fabrication. The matrix material used in the present study is a mixture of epoxy-based resin Araldite® CY230 and hardener Araldite® HY951 in the ratio of 10:1, respectively. After the hand layup process, the laminate is allowed to cure for 24 h under vacuum. After the curing process, the specimens are cut as per the required dimensions, and the fiber volume fraction is ≈ 55%. Table 1 and Table 2 summarize the stacking sequence and dimensions of different laminates considered to evaluate the intra-laminar and inter-laminar damages, respectively, using the AE and DIC techniques. Fig. 1 shows the schematic of tensile test specimens and the fiber orientation with respect to the loading direction. According to ASTM D3039 standard [64], the tensile specimen are tested for intra-laminar damage characterization. In addition, specimens are fabricated as per ASTM D5528 [65], ASTM D7905 [66], and ASTM D6671 [67] standards for mode-I, mode-II, and mixed-mode delamination failures.

2.2. Experimental testing

A 100 kN MTS universal testing machine (UTM) (for UD0 specimens) and a 10 kN quasi-static INSTRON UTM (for all other specimens) are used for the testing of specimens. The specimens are loaded at a rate of 1 mm/min under displacement control, and the experiments are conducted at room temperature. Fig. 2 shows the experimental setup involving the INSTRON testing machine, DIC, and AE.

In this study, two wideband piezoelectric AE sensors (WSα) from Physical Acoustics Corporation with an operating frequency range of 100–1000 kHz and a peak sensitivity at 55 dB are used as shown in Fig. 2. The signals captured by the sensors are amplified using a 2/4/6-AE preamplifier with a gain setting of 40 dB. A threshold of 35 dB is used to remove the unwanted noise in the AE signal. The AE setup is calibrated using the standard pencil lead break test before the actual test. The acquired signals by the sensors
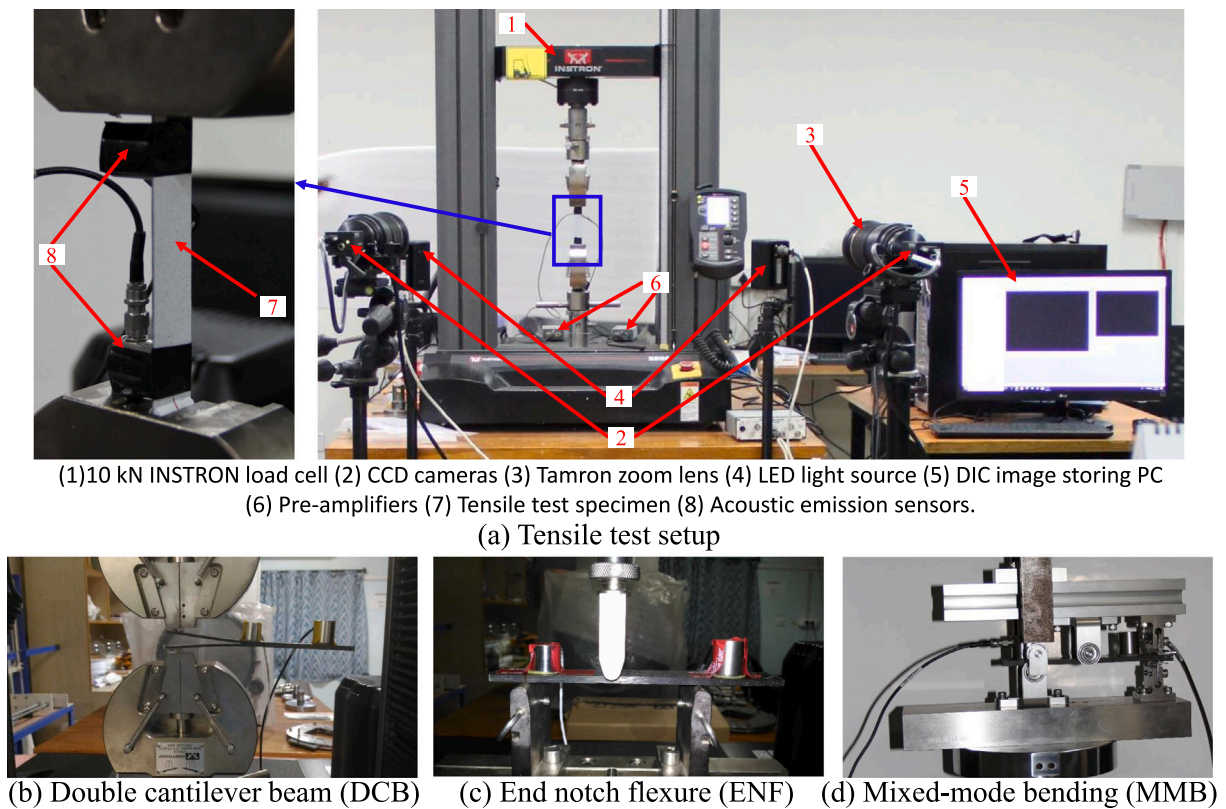
(1)10 kN INSTRON load cell (2) CCD cameras (3) Tamron zoom lens (4) LED light source (5) DIC image storing PC
(6) Pre-amplifiers (7) Tensile test specimen (8) Acoustic emission sensors.
(a) Tensile test setup

(b) Double cantilever beam (DCB) (c) End notch flexure (ENF) (d) Mixed-mode bending (MMB)

Fig. 2. Experimental setup involving AE and DIC techniques for intra/inter-laminar damage characterization.

are stored in a computer using the AE data acquisition card with a sampling frequency of 10 MHz. The signals are filtered through a bandpass filter of frequency range 20 kHz to 1000 kHz. Later, the AE data is post-processed using AEwin software (MISTRAS Group, Inc.) to identify and distinguish various damages in the specimen. Besides, a 3D DIC technique is used to obtain the whole-field displacement and strain field on the surface of the specimen. The 3D-DIC system consists of two Grasshopper® charge-coupled device (CCD) cameras (Point Grey-Grass-5055M-C), and they are integrated with Tamron zoom lens (see Fig. 2). White paint is applied over the surface of the specimen, and a random speckle pattern is sprayed using an airbrush to perform the DIC measurements. Two LED light sources of 50 W capacity are used to illuminate the specimen surface. Stereo calibration is used for calibrating the DIC cameras with a uniformly spaced dot pattern with 7 mm spacing. The calibration target is imaged simultaneously in both cameras, and the synchronized target images are used to calibrate the system [68]. The Vic-Snap software from Correlated Solutions Inc (Columbia, SC, USA) is used to capture the images of the test specimen at a rate of 2 frames per second with a spatial resolution of 4096 × 3000 pixels. Subsequently, the images are stored in the computer and post-processed using Vic-3D 7 software to obtain the whole-field surface displacement and strain fields. A subset size of 33 × 33 pixels is used with a step size of 3 pixels for performing the DIC post-processing. For the strain calculation, a filter size of 5 pixels is used. All the contour plots are visualized with an opacity of 100% in the color map option available in the software.

3. Experimental results

The force–displacement response of the specimens that characterize the intra-laminar and inter-laminar failure are shown in Figs. 3 and 4, respectively. The force–displacement response of UD90 laminate shown in Fig. 3(a) is initially linear, with multiple load drops observed in all the specimens. The primary failure in the UD90 laminate is the matrix failure, which initiates due to fiber–matrix debonds. After the matrix failure, the glass fibers that hold the carbon tows in place support the load and lead to multiple load drops. Fig. 3(b) shows the force–displacement response of the UD45 laminate for all the specimens. The force–displacement curve is nonlinear due to the matrix shear nonlinearity.

The force–displacement response of the Q±45 specimen shown in Fig. 3(c) is nonlinear, and stiffness reduction is observed at ≈ 1600 N. The damage initiates at a load of 1600 N, and its progression occurs gradually till the peak load of 2700 N. Fig. 3(d) shows the force–displacement response of UD0 laminate with the same stiffness for all the specimens. Initially, fiber failure occurs in clusters at random locations in the specimen, and the final failure in the specimen is sudden due to the cumulative effect of all the cluster failures.
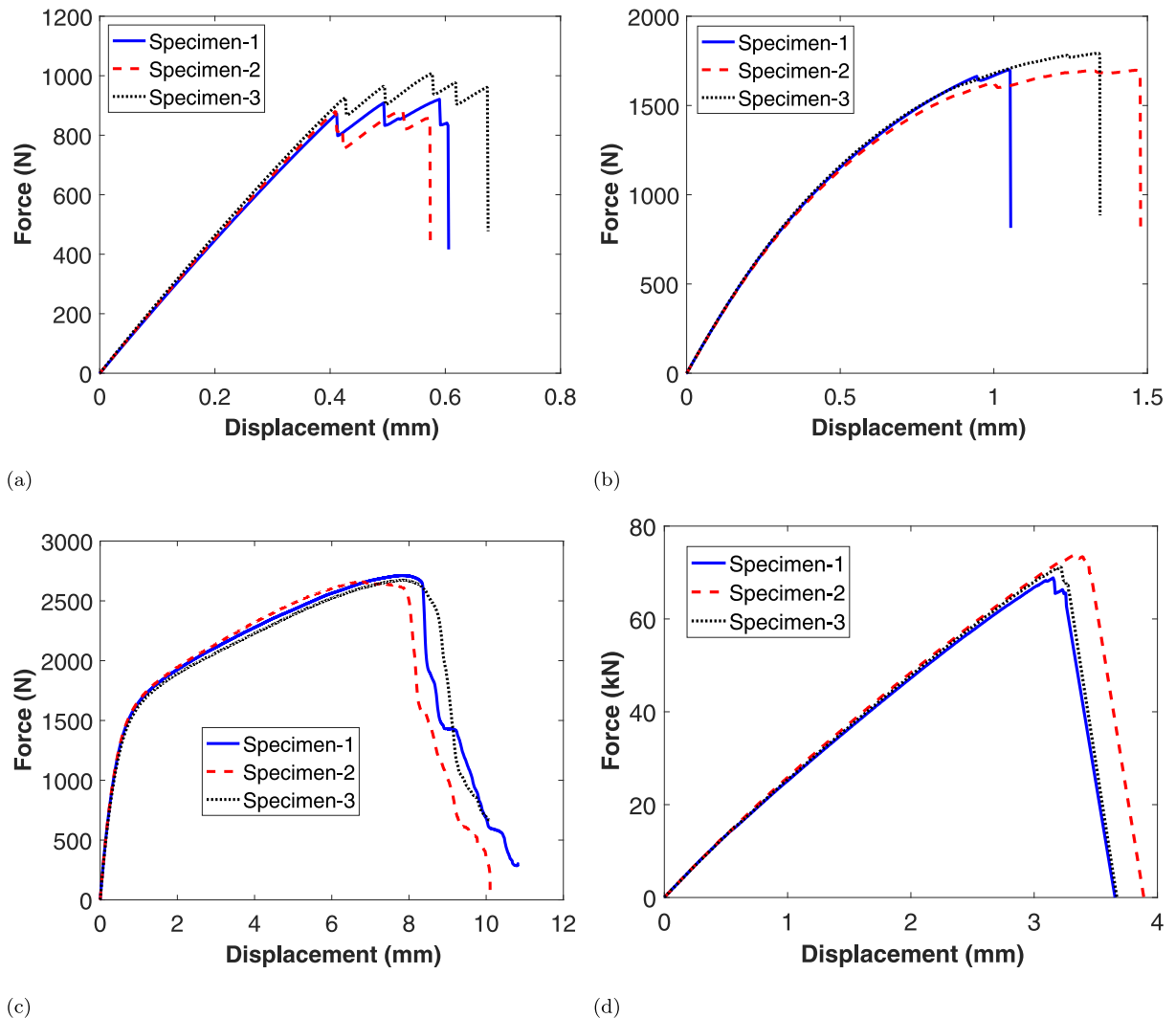
Fig. 3. Force–displacement response of the specimens subjected to tensile loading. (a) UD90 (b) UD45 (c) Q±45 (d) UD0.

Fig. 4 shows the force–displacement response of the DCB, ENF, and MMB specimens. For the DCB specimen, the force–displacement response is initially linear and becomes nonlinear before reaching the peak load (see Fig. 4(a)). After the first load drop, the force–displacement response shows the stick–slip behavior in all the specimens. This is due to the misalignment of fibers and fiber bridging, which arrests the crack propagation and results in multiple load drops. The force–displacement response of ENF specimen under three-point bending is shown in Fig. 4(b). The response is linear until the load reaches the maximum value, and the delamination propagates suddenly, leading to a sharp load drop. The force–displacement response of the MMB specimen is shown in Fig. 4(c). In this study, the test specimen configuration is loaded with the % mode ratio ($\frac{G_{II}}{G_T} = 50\%$). Initially, the force–displacement response is linear and changes to nonlinear before reaching the peak load, where the delamination starts propagating. The force–displacement response shows a similar stick–slip behavior observed in DCB but with a very sharp load drop compared to ENF results.

4. Classification of AE events

4.1. k-Means: unsupervised clustering

In this study, an unsupervised machine learning algorithm, namely, k-means clustering algorithm [69] is used to study the AE signals. The k-means algorithm is an efficient and popular method for data clustering but requires the number of clusters as input for analyzing AE data. Also, the knowledge of damage evolution is required to assign physical meaning to the obtained clusters.
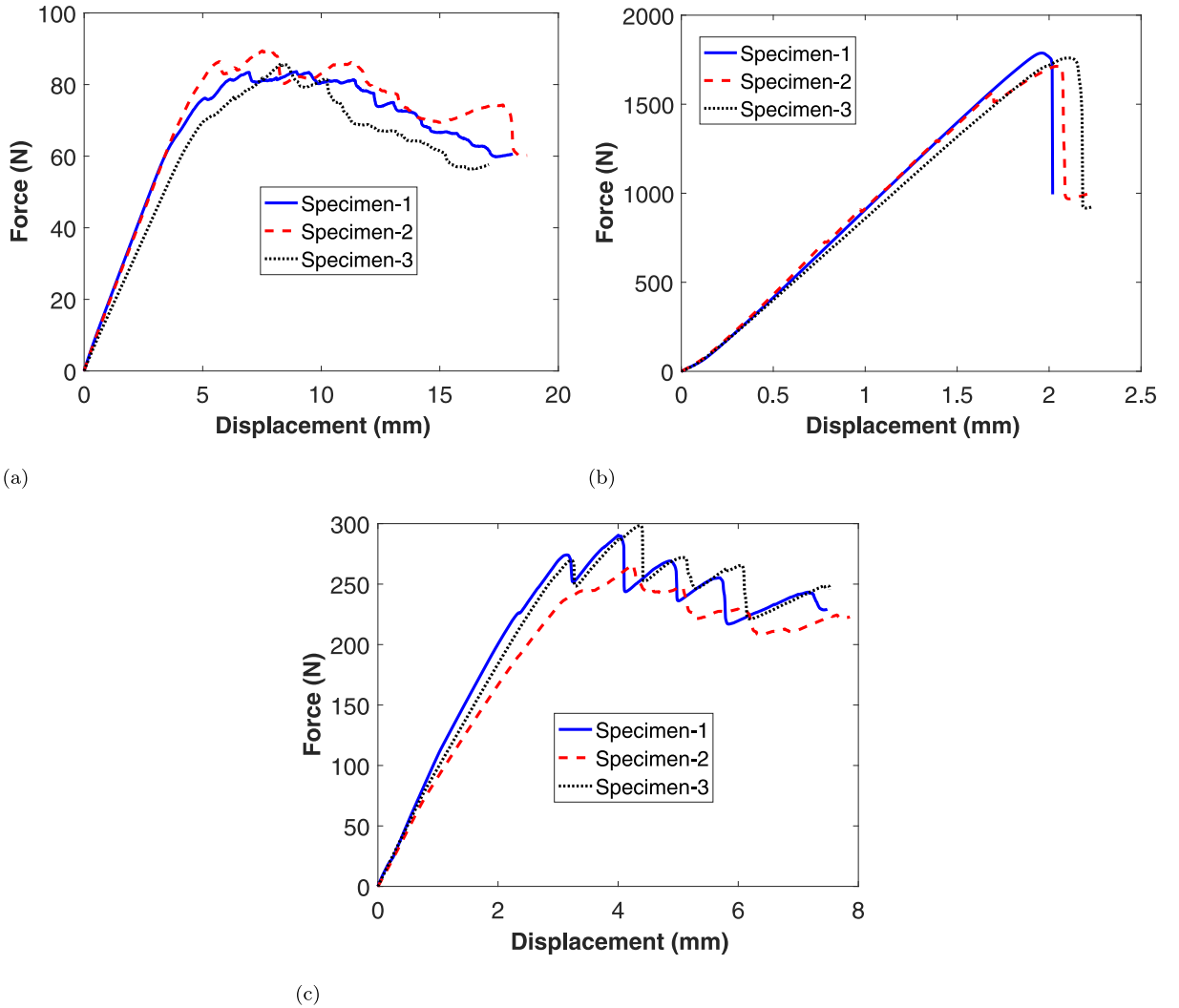
Fig. 4. Force–displacement response of the specimens considered to characterize inter-laminar delamination. (a) DCB (b) ENF (c) MMB.

4.2. Feature selection and optimum number of clusters

In this study, the AE parameters, namely, the amplitude and peak frequency are used in the k-means clustering technique [70–72]. The Elbow Method, Silhouette Index, and Davies–Bouldin Index are used to determine the optimum number of clusters for analyzing the AE data.

The Elbow method index is the sum of squared error (SSE) and is given by

$$SSE = \sum_{i=1}^{k} \sum_{q \in C_i} |q - m_i|^2 \tag{1}$$

where C_i is the ith cluster, q is the data point of C_i, and m_i is the centroid of C_i that denotes the mean value of all points [58].

The Silhouette score for each specimen is calculated using the following expression

$$S_i = \frac{b_i - a_i}{max(a_i, b_i)} \tag{2}$$

where a is the average intra-cluster distance, and b is the average inter-cluster distance [38,54]. The Silhouette index/score varies between −1 to +1, and the highest value shows good similarity to its own cluster and poorly matches to other clusters.

The Davies–Bouldin index is evaluated using the following expression

$$DB = \frac{1}{k} \sum_{i=1}^{k} D_{i,j}, \quad D_{i,j} = \frac{\bar{d}_i + \bar{d}_j}{d(c_i, c_j)} \tag{3}$$
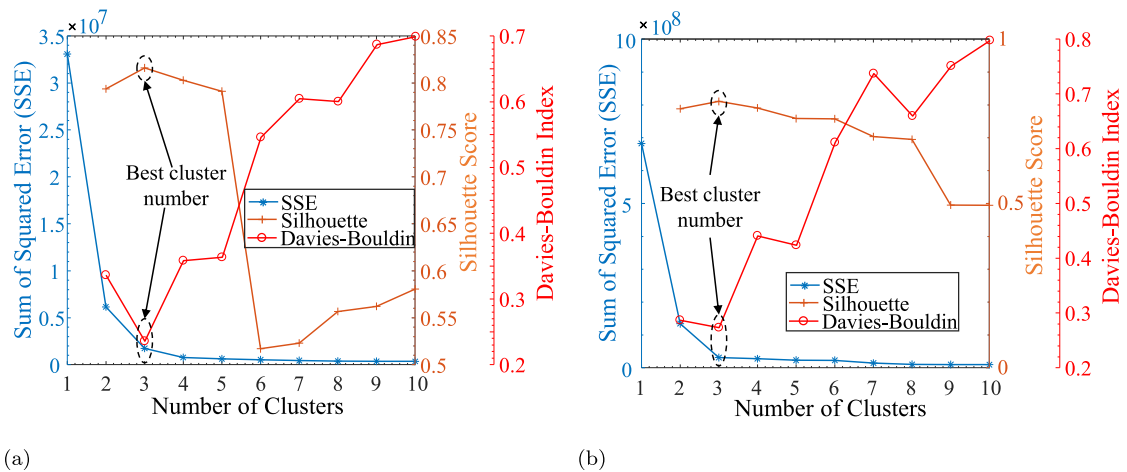
Fig. 5. Optimum number of clusters for composite specimens evaluated using different indices. (a) UD90 specimen (b) DCB specimen.

where $D_{i,j}$ is the within-to-between cluster distance ratio for the ith and jth clusters [38,56].

Fig. 5 shows the SSE, Silhouette score, and Davies–Bouldin index variation with the number of clusters for UD90 and DCB specimens (see Appendix for remaining specimens data). The plots show that the SSE and Davies–Bouldin index is low, and the Silhouette score is high when the number of clusters is equal to three. The optimum number of clusters depends on the type of specimen tested and the damages that occurred in the laminate under different loading conditions. Most of the studies reported the optimum number of clusters to be four [14,30,58] and few studies stated three clusters [20]. In this study, the specimens are considered such that the failures are limited to a minimum number. Thus, the results from this study conclude that three clusters are sufficient to differentiate AE events for all the specimens.

4.3. Clustering of AE data using k-means

Fig. 6 shows the clustered AE signals of all the specimens considered to characterize the intra-laminar damage. In the UD90 and UD45 specimens, the failure happens locally, and it is governed by matrix damage resulting in more events in clusters 1 and 2. Also, the number of events in cluster-3 is less in UD45 laminate compared to UD90 laminate. In Q±45 and UD0 laminates, a higher density of events is observed in all the clusters as all the damage modes are distributed throughout the specimen.

The clustered AE data based on amplitude and peak frequency for the inter-laminar failure specimens is shown in Fig. 7. In all these specimens, delamination is the dominant damage mode compared to other failures. Also, more AE events are observed in the DCB and MMB specimens compared to the ENF specimen.

Table 3 summarizes the peak frequency and amplitude range of three clusters of laminates considered to characterize the intra/inter-laminar damage modes. In cluster-1, hits greater than 58 kHz are observed for all specimens. So, the minimum frequency range for cluster-1 is considered as 58 kHz. The maximum frequency range for cluster-1 is obtained as 175 kHz. For clusters 1 and 2, there is no overlap region. However, for clusters 2 and 3, an overlap region of 29 kHz is observed (390 kHz to 419 kHz). The events in this region are very low, and the average value of 400 kHz is considered at the boundary of clusters 2 and 3. Only in the specimens where the fiber failure is dominant (UD0 specimen), the events with peak frequency up to 1000 kHz are observed. Similarly, the amplitude ranges for clusters 1, 2, and 3 are summarized as 35–75 dB, 35–75 dB, and 35–95 dB, respectively.

The ranges of AE parameters for different damages depend on factors like fiber and matrix material properties, composite manufacturing process, stacking sequence, type of loading, sensor type, sensor placement, etc. Even though there is no clear picture of the amplitude ranges for different failures, there are some commonly accepted ranges for peak frequency for different types of damage. The matrix failure has the lowest frequency range, whereas fiber failure has the highest frequency range. The failures like delamination and debonding have a frequency range between matrix and fiber failure [36,37].

5. Damage identification

Once the AE data is clustered, assigning each cluster to its respective damage is very challenging. At first, it is necessary to understand the damage modes and the failure mechanisms that occur in the laminates. In this section, the surface displacement and strain data of the laminate evaluated using DIC and the fractography studies on the post-failure specimens are analyzed to understand the failure mechanisms in composite laminates. This study helps in assigning the damage modes to the cluster results obtained in the previous section.

The DIC images are post-processed, and the variation of longitudinal displacement and strain (ε_{xx}) contours in the region of interest (ROI) within the gauge length at different load levels for the UD90 specimen are shown in Fig. 8. In this study, the global
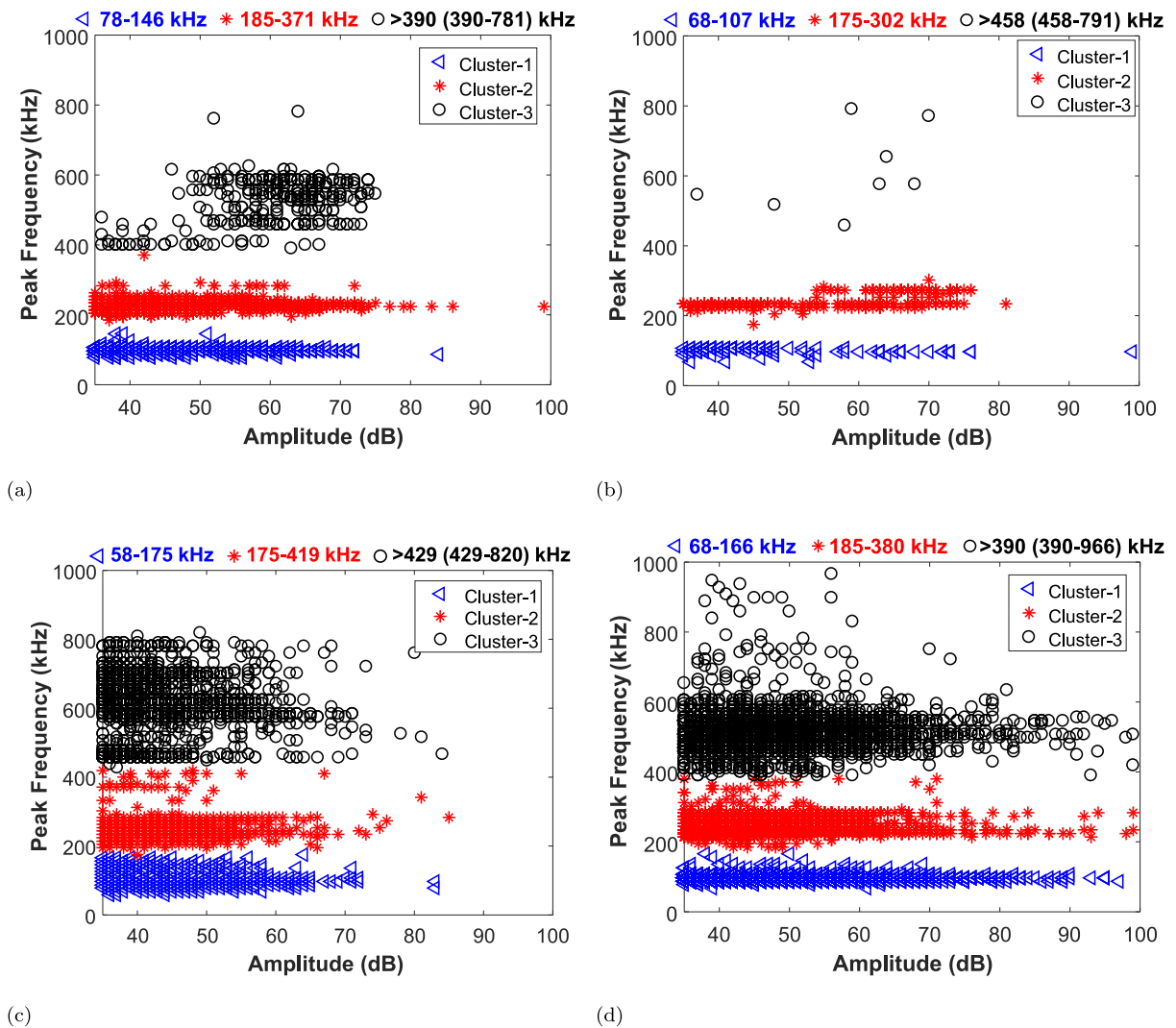
Fig. 6. Clustered AE signals for different specimens subjected to tensile load. (a) UD90 (b) UD45 (c) Q±45 (d) UD0.

Table 3

Summary of peak frequency and amplitude ranges of the clusters for different laminates obtained using *k*-means clustering.

Laminate type	Optimum number of cluster	Cluster peak frequency ranges (kHz)			Cluster amplitude ranges (dB)		
		Cluster-1	Cluster-2	Cluster-3	Cluster-1	Cluster-2	Cluster-3
UD90 ($[90^0]_8$)	3	78–146	185–371	390–781	35–75	35–75	50–75
UD45 ($[45^0]_8$)	3	68–107	175–302	458–791	35–75	35–75	–
Q±45 ($[\pm45^0]_{2s}$)	3	58–175	175–419	429–820	35–75	35–75	35–70
UD0 ($[0^0]_8$)	3	68–166	185–380	390–966	35–90	35–90	35–95
DCB	3	68–166	175–371	380–888	35–75	35–65	35–75
ENF	3	78–146	205–371	400–625	35–65	35–70	35–70
MMB	3	58–166	175–380	390–908	35–75	35–75	35–80
Min-Max		**58–175**	**175–400**	**400–966**	**35–75**	**35–75**	**35–95**

and local coordinate systems are designated as *x*, *y*, *z* and 1, 2, 3 axes, respectively, to represent the strain field evaluated on the surface of the specimen. Fig. 8(a) shows the axial displacement contour at different load steps. With the increase in load, the variation in displacement contour is observed due to the damage evolution along the 90^0 fiber direction (perpendicular to the loading direction). Fig. 8(b) shows the axial strain (ε_{xx}) contours with strain localization happening at multiple locations along the length of the specimen. Finally, failure occurs locally at the top region of the specimen, which has a higher strain concentration.
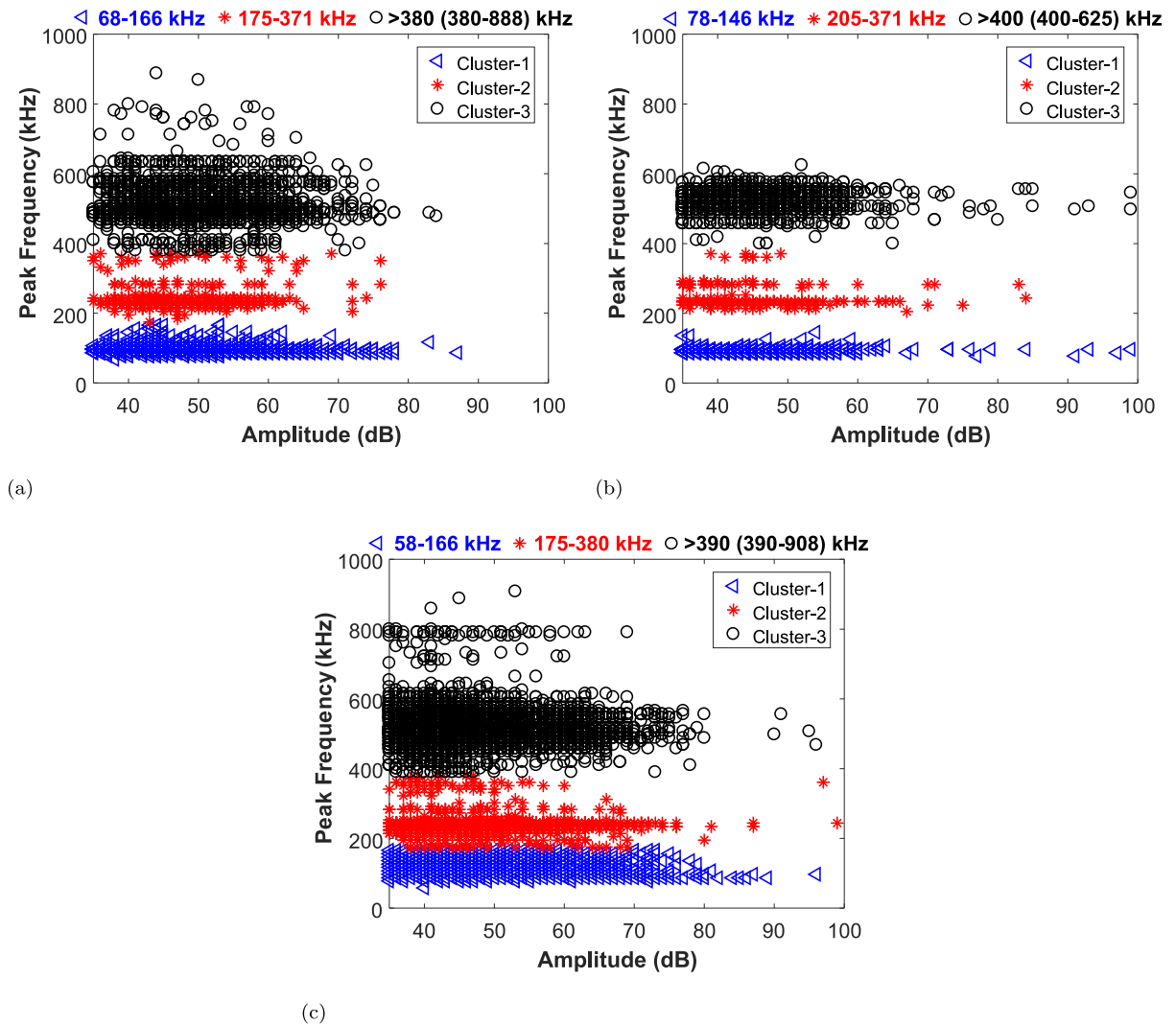
Fig. 7. Clustered AE signals for different specimens studied to characterize delamination failure. (a) DCB (b) ENF (c) MMB.
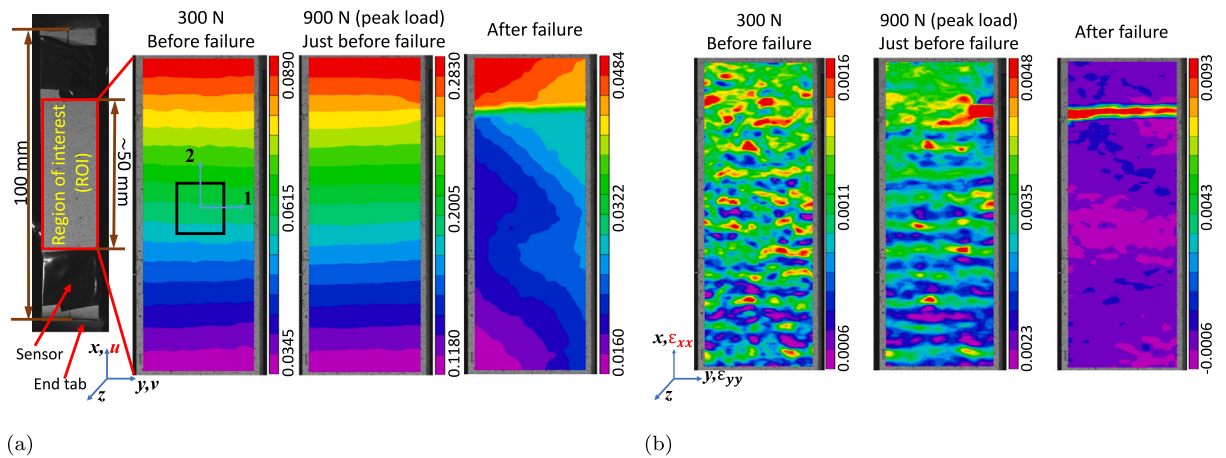

Fig. 8. Displacement and axial strain contours on the surface of the specimen for UD90 specimen. (a) Longitudinal displacement contour (u in mm) (b) Axial strain contour (ε_{xx} in micro strain ($\mu\varepsilon$)).

(a) Initiation and propagation of two matrix cracks

(b) Interaction of two matrix cracks causes fiber failure

(c) Microscopic images of failure in UD90 specimen

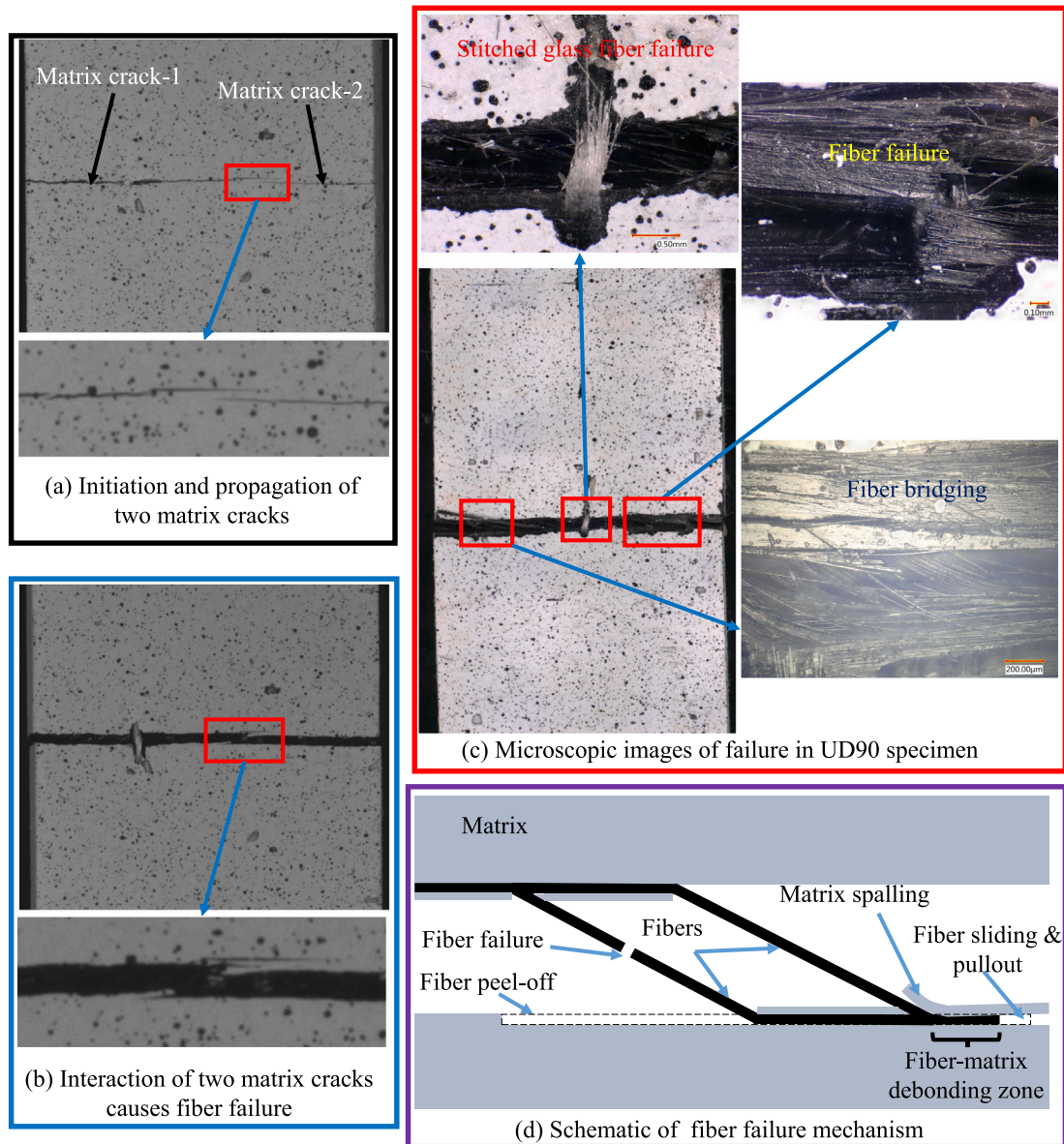(d) Schematic of fiber failure mechanism

Fig. 9. Failure mechanism in UD90 laminate subjected to tension.

Further, the images captured by the DIC cameras for the UD90 specimen at two different time frames show the matrix cracks in Fig. 9. These matrix cracks are termed as transverse cracks as they initiate at the edges of the specimen at different heights and propagates towards the middle of the specimen due to fiber–matrix debonding (see Fig. 9(a)). Later, the transverse cracks interact with each other and results in fiber peel-off failure, as shown in Fig. 9(b).

In addition, fractography studies are carried out on the failed UD90 specimen, and the results are shown in Fig. 9(c). The failure in the specimen is governed by matrix cracking and fiber–matrix debond throughout the thickness of the laminate. Here, the unidirectional carbon fabric consists of glass fiber at regular intervals in the transverse direction to keep the tows aligned along the longitudinal direction. As the loading direction is transverse to the carbon fiber direction, the glass fibers are parallel to the loading direction and they support the tensile load after the matrix failure occurs. The failure of glass fiber strands produces AE hits with high frequency that is observed after the first load drop. The contact between the top and bottom part of the specimen is not entirely lost after the first load drop, and they are held through fiber bridging [73]. The schematic of fiber bridging phenomenon due to the nesting of the fibers and fiber–matrix debonding is shown in Fig. 9(d) [74,75].

Fig. 10 shows the axial displacement and strain (ε_{xx} and ε_{xy}) contours for UD45 specimen before and after failure. The axial iso-displacement contour plots shows the gradient of displacement in the width direction along the length of the specimen. This
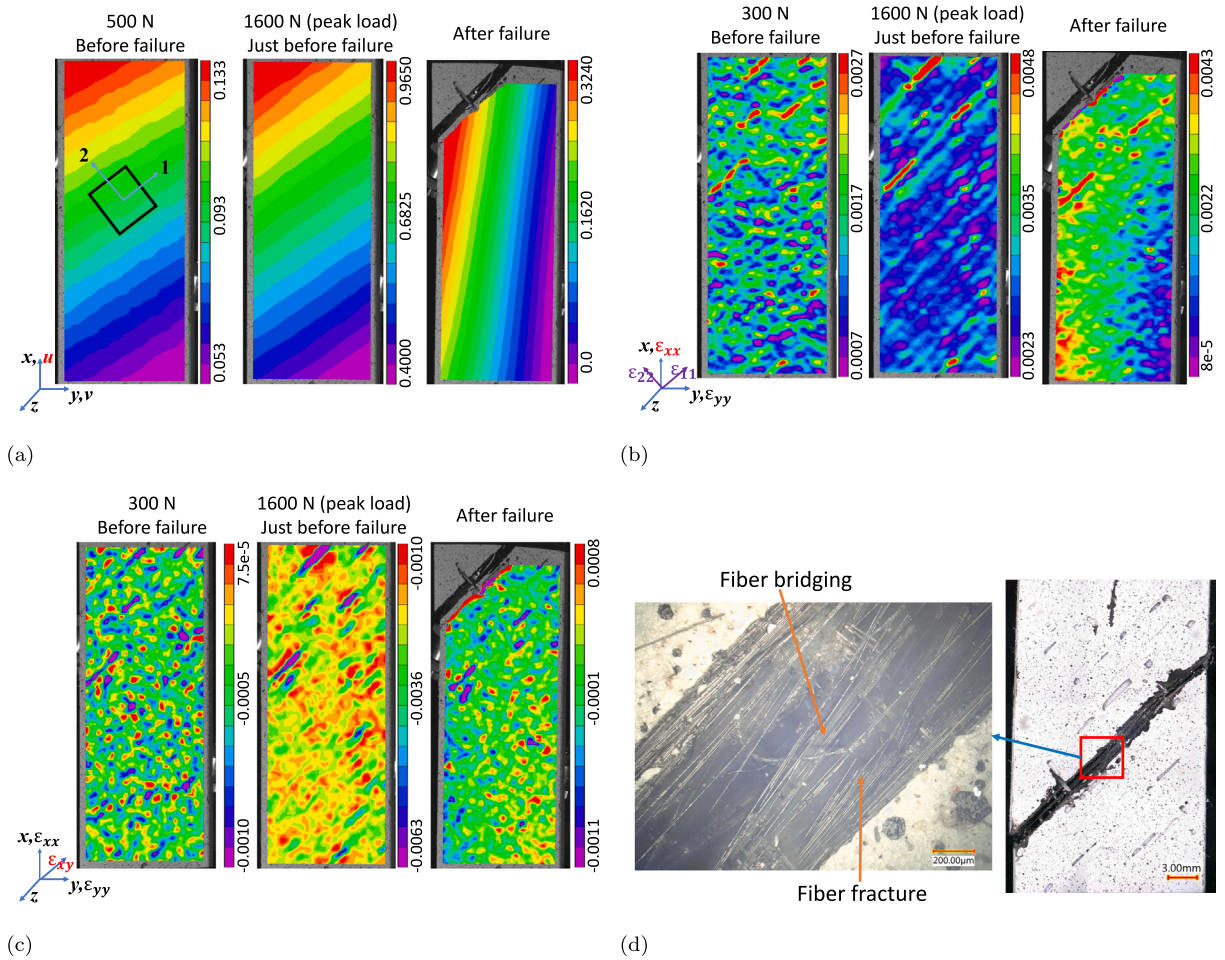
Fig. 10. Displacement and strain field on the surface of the specimen and failure in UD45 specimen. (a) Longitudinal displacement contour (u in mm) (b) Longitudinal strain contour (ε_{xx} in $\mu\varepsilon$) (c) Shear strain contour (ε_{xy} in $\mu\varepsilon$) (d) Failure mechanism in UD45 specimen.

deformation is attributed to the presence of extension-shear coupling in the laminate. Figs. 10(b) and 10(c) shows the non-uniform axial and shear strain distribution in the specimen with strain concentration observed along the 45^0 fiber directions. The magnitude of shear strain is more compared to the axial strain when transformed to the material coordinate system, and the failure is governed by the complex biaxial strain in the specimen. The failure mechanism of UD45 laminate is shown in Fig. 10(d), and it is due to fiber–matrix shear failure along the 45^0 fiber direction. Also, some amount of fiber bridging is observed between the top and bottom parts of the specimen, as seen in Fig. 10(d).

For Q±45 specimen, the longitudinal displacement and strain (ε_{xx} and ε_{xy}) contours at different load levels are shown in Fig. 11. The axial displacement contour is uniform along the laminate width due to the symmetric arrangement of $+45^0$ and -45^0 plies in the specimen. The strain distribution is heterogeneous and shows strain concentration along the $+45^0$ and -45^0 directions. This is due to the matrix failure and fiber–matrix debonding happening in the $+45^0$ and -45^0 lamina throughout the length of the specimen. The matrix failure is shear dominated and subsequently interacts with the delamination between the $\pm45^0$ plies resulting in the final failure of the laminate. The fractography results shown in Fig. 11(d) also supports the above observations.

Fig. 12 shows the longitudinal displacement, axial strain (ε_{xx}) contour plots, and the failure evolution in UD0 laminate at different load levels. With the increase of load, the localized changes in displacement contour show the damage evolution in the laminate. In UD0 laminate, the fiber fracture happens in small clusters at low loads, and as the load increases, they do not grow into large clusters (see Fig. 12(c)). Instead, these clusters happen at random locations, and the damage events remain localized. Also, there is no clear understanding on the roles of matrix failure and fiber–matrix debonding in the transfer of loads from the broken fibers to the adjacent intact fibers. Later, the failure in local clusters interacts with each other and leads to catastrophic failure of the specimen. Further, DIC results are shown partially in the specimen as it becomes difficult to perform DIC correlation in certain regions due to fiber splitting failure in the laminate. The longitudinal strain ε_{xx} shows strain concentration along the width of the laminate, and this is attributed due to the presence of glass fibers transverse to the carbon tows. Due to this, resin-rich areas form
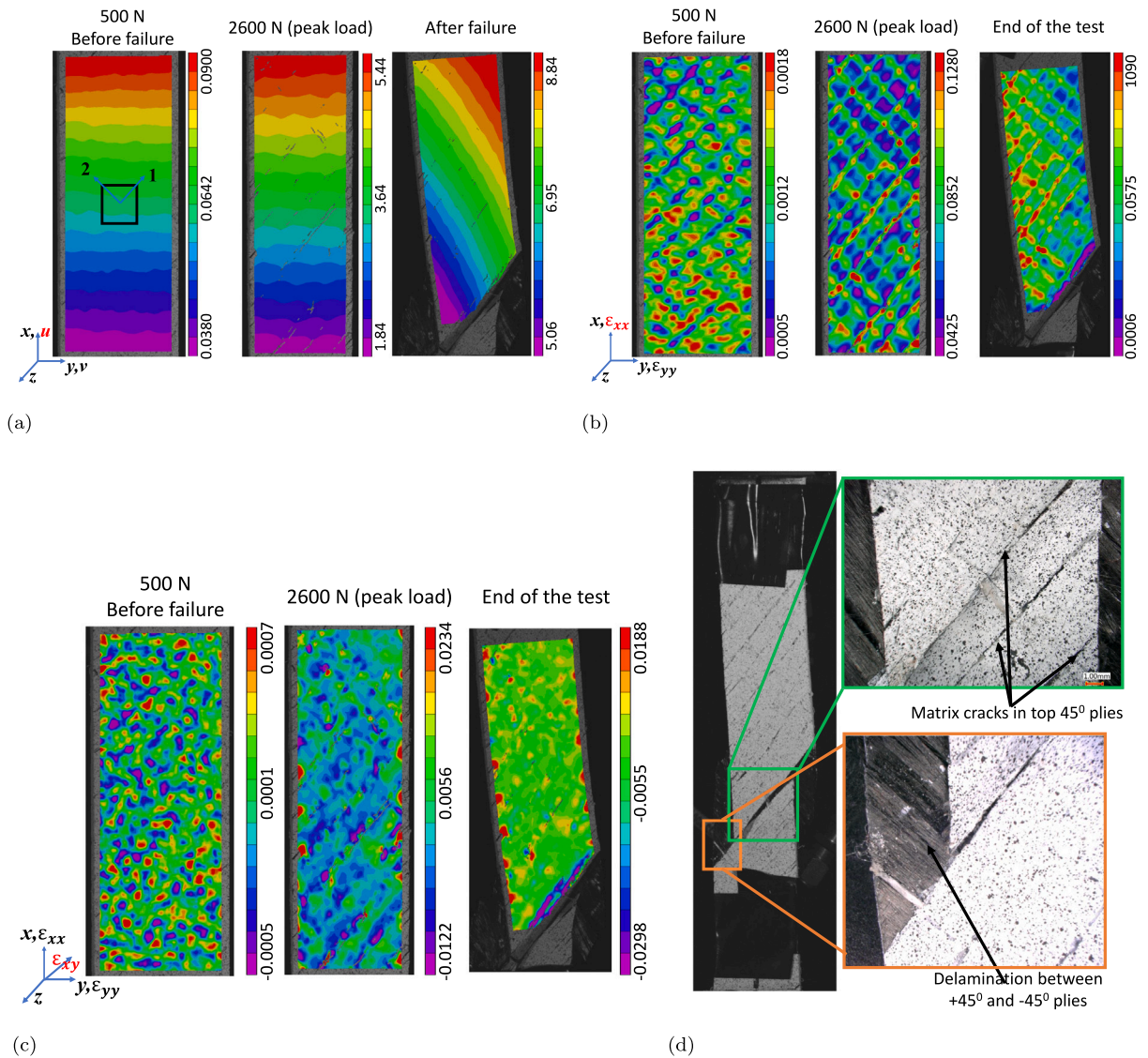
Fig. 11. Displacement and strain field on the surface of the specimen and failure in Q±45 specimen. (a) Longitudinal displacement contour (u in mm) (b) Longitudinal strain contour (ε_{xx} in $\mu\varepsilon$) (c) Shear strain contour (ε_{xy} in $\mu\varepsilon$) (d) Failure mechanism in Q±45 specimen.

locally, lead to less fiber volume fraction in the loading direction, and result in high strain values compared to the adjacent regions of the specimen.

Fig. 13(a) shows the micrographs of delaminated surface in DCB specimen under mode-I loading. The micrographs show that, apart from delamination, fiber bridging failures like fiber failure and fiber peel-off (see Fig. 13(a)) are observed. Fig. 13(b) shows the delaminated surface in the ENF specimen under a three-point bending load. The failure surface observed in mode-II delamination due to inter-laminar shear is smoother than the DCB specimen micrograph (mode-I delamination).

6. Damage classification

DIC and fractography observations show that the failures in UD90 and UD45 are governed by matrix damage and fiber–matrix debond, which helps in assigning the frequency ranges 58–175 kHz and 175–400 kHz with the micro/macro matrix cracking and fiber–matrix debonding, respectively. The amplitude range of these two clusters is observed to be the same as 35–75 dB. The cluster-3 events predominantly represent delamination failure (using ENF specimen), and it is associated with peak frequency range of 400–600 kHz with corresponding amplitude range of 35–70 dB. The frequency range > 600 kHz belongs to the fiber failure, and this range of hits are observed primarily in UD0 laminate (see Fig. 6(d)), with an amplitude range of 35–60 dB.
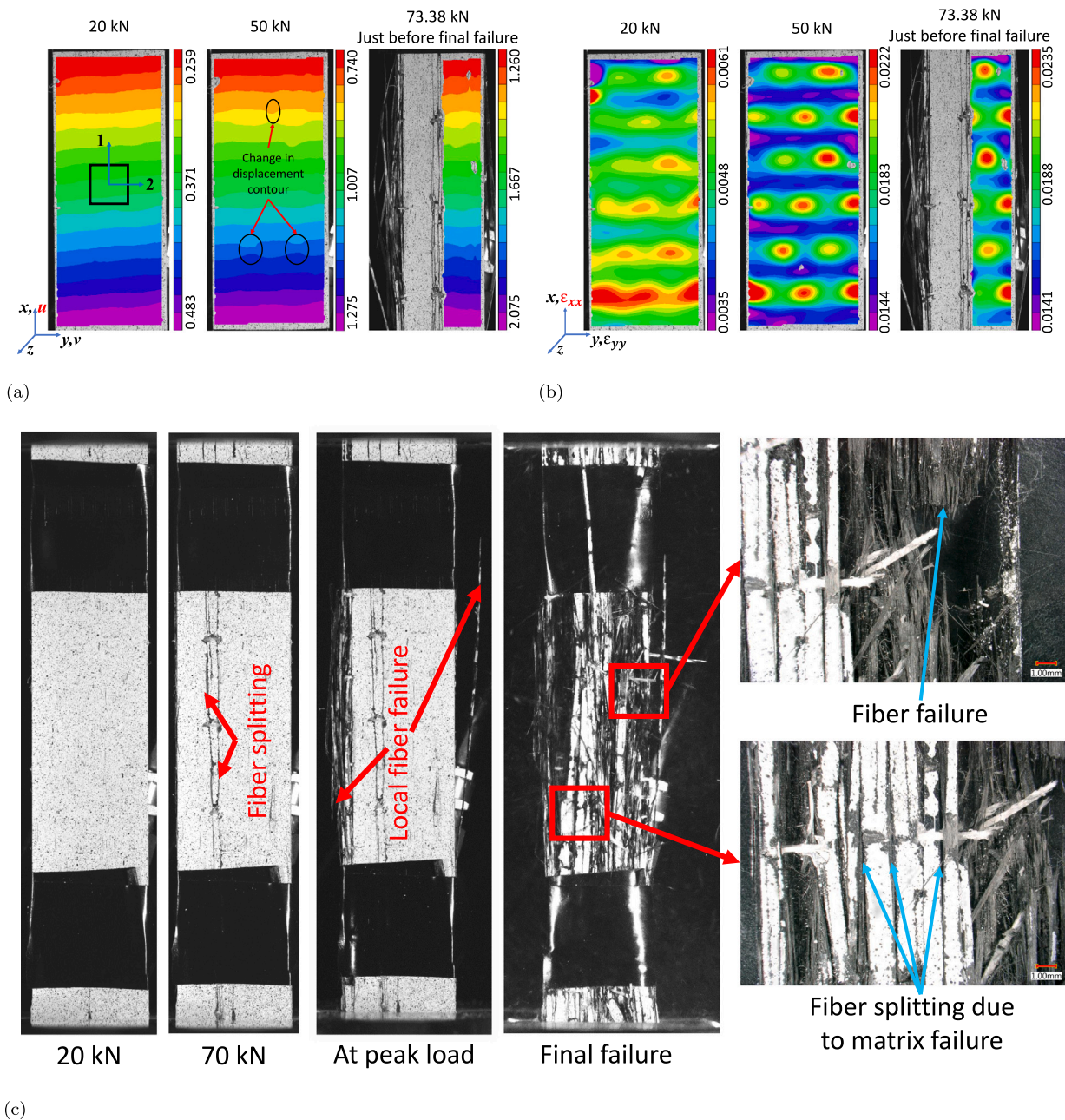
Fig. 12. Displacement and strain field on the surface of the specimen and failure in UD0 specimen. (a) Longitudinal displacement contour (u in mm) (b) Longitudinal strain contour (ε_{xx} in $\mu\varepsilon$) (c) Failure mechanism in UD0 specimen.

There is no evidence of delamination in UD90, UD45, and UD0 specimens, but it still shows events in the cluster-3 frequency range of 400–600 kHz. This corresponds to failures like fiber peel-off and pullout in the UD90, UD45, and UD0 specimens. The amplitude range for fiber peel-off damage observed from UD90 and UD45 is 50–75 dB, and fiber pullout from UD0 is 35–95 dB. The summary of the range of peak frequency and amplitude of each damage mode is shown in Fig. 14.

7. Results and discussion

The results in the previous section show the capabilities of combining AE and DIC in discriminating different damage modes using AE parameters. In this section, the failure initiation strain and the cumulative energy of different failure modes for all the specimens are evaluated, which can assist in developing progressive damage models for composite laminates.
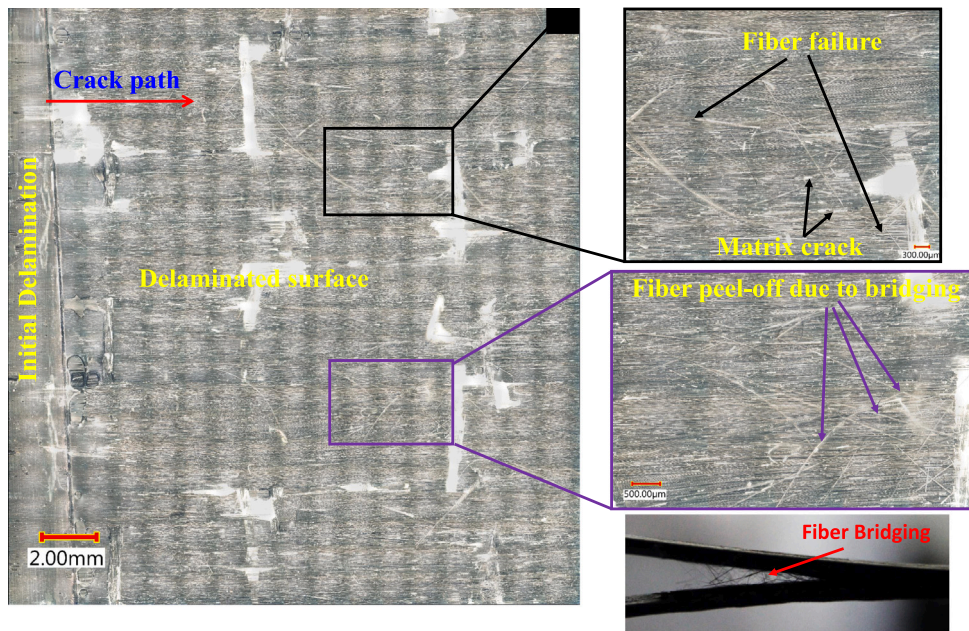
(a)
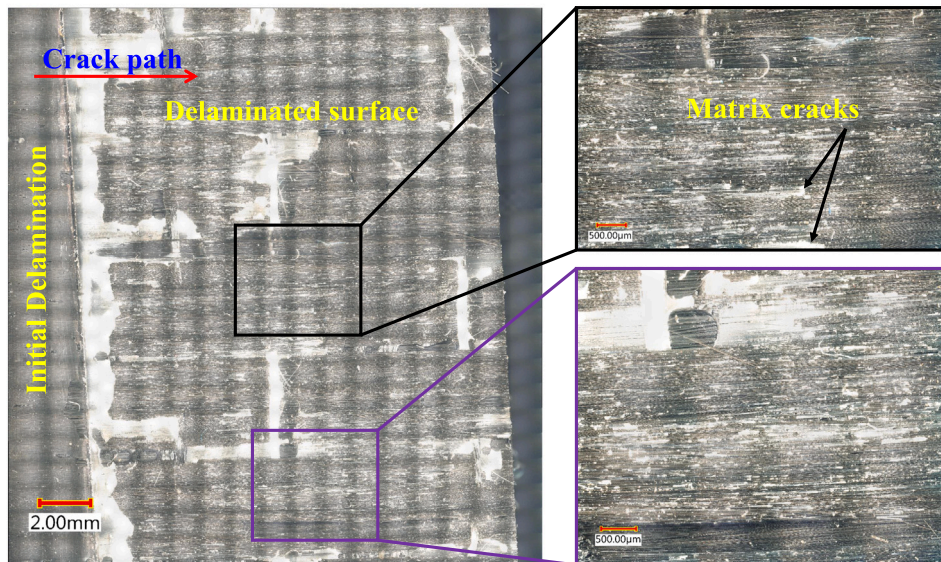
(b)

Fig. 13. (a) Micrographs of delaminated surface in DCB specimen and fiber bridging. (b) Micrographs of delaminated surface in ENF specimen under bending.

7.1. Intra-laminar failure

Fig. 15 shows the variation of in-plane strain components in the local coordinate system (ϵ_{11}, ϵ_{22} and ϵ_{12}) and cumulative energy of different failure modes with respect to the applied displacement. In UD90 specimens, the strain and the cumulative energies are considered till the first load drop as it represents the transverse matrix failure. The strains are averaged over a small area (see Fig. 8(a)) in the central region of the specimen and transformed into the material coordinate system for understanding strain evolution. The variation of strains and the cumulative AE energy of different clusters with respect to the applied load is shown in Fig. 15(a). The strain ϵ_{22} variation is almost linear, and it is high compared to other strains. The cumulative energy of the matrix
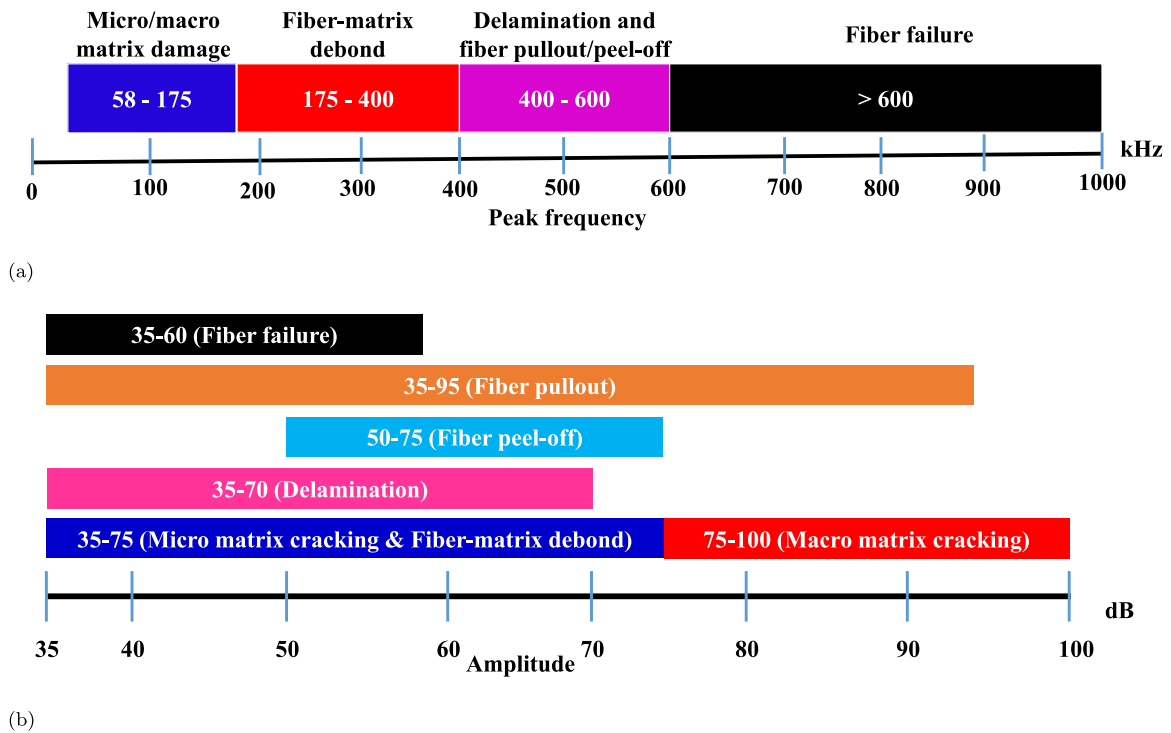
Fig. 14. Range of AE parameters for different damage modes in CFRP composite laminate. (a) Peak frequency (b) Amplitude.

damage is high compared to the other damage modes, and the steep rise in AE energy corresponds to the transverse matrix cracking in the UD90 specimen with a failure strain magnitude of 3500 $\mu\varepsilon$.

In the case of UD45 specimen, the variation of strains ε_{12} and ε_{22} is shown in Fig. 15(b). The shear strain and axial strain to fracture is about 6000 $\mu\varepsilon$ and 3500 $\mu\varepsilon$ respectively. The cumulative energy of the matrix failure is very high, which is observed at the load drop. The failures in the UD90 and UD45 specimens are localized, but their failure mechanisms are different due to the presence of different stress states in the laminates.

Fig. 15(c) shows the variation of in-plane strain components and cumulative energy of different failure modes with respect to the applied displacement. Only shear strain ε_{12} is present, and strains ε_{11} and ε_{22} are zero, which shows that the specimen is subjected to pure shear. It is observed that the specimen is subjected to a large strain ($\approx$ 9% of shear strain), which leads to significant fiber angle rotation (fiber rotation of 1^0 takes place for every 3.5% of shear strain). Due to this, ASTM D3518 [76] suggested calculating all the measurements by considering the data to 5% of strain. So, the cumulative energy for different failures is considered till 5% of shear strain. Three critical points A, B, and C are marked on the force–displacement response (see Fig. 15(c)), which corresponds to different failures in the laminate. At point A, a sudden jump in the cumulative energy is observed due to matrix failure in the $\pm$ 45^0 lamina and reduces the stiffness of the laminate. The shear strain at this point is evaluated as $\approx$ 6000 $\mu\varepsilon$, which is same as the failure strain in the case of UD45 laminate. This shows that the failure shear strain ε_{12} for matrix damage is $\approx$ 6000 $\mu\varepsilon$. Later, the load increases till point B, and the delamination failure between $+45^0$ and -45^0 plies initiate without any change in the stiffness. At point C, the strain decreases, multiple matrix cracks are observed in the laminate (along 45^0), and the delamination propagates between $+45^0$ and -45^0 plies in the laminate. After reaching maximum load (point C), the fiber/matrix failure occurs in the laminate leading to the final load drop. The cumulative energy for matrix damage and fiber–matrix debond are high compared to the other failures, showing that the damage is governed by matrix-related failure in the specimen.

The variation of strains and cumulative energy with respect to the applied load for the UD0 specimen is shown in Fig. 15(d). The final failure of the specimen occurs at a strain (ε_{11}) of $\approx$ 20 000 $\mu\varepsilon$ (2% of axial strain), which is significantly high compared to the other damage modes. The cumulative energy for fiber failure is shown as the other damages do not lead to stiffness/strength degradation. The cumulative energy increases continuously due to multiple fiber breaks at the different locations in the specimen.

7.2. Inter-laminar damage

Fig. 16(a) the cumulative energy for different failures in DCB, ENF, and MMB specimens. In DCB, no events are observed until the initiation of delamination. The increase in cumulative energy for all failures is observed with delamination propagation. As the delamination propagates, the fiber bridging occurs (see Fig. 13(a)) due to the nesting of fibers in the DCB specimen, which results in other failures. Nesting of fibers is common in unidirectional lay-ups during the curing process, and this results in a meandering
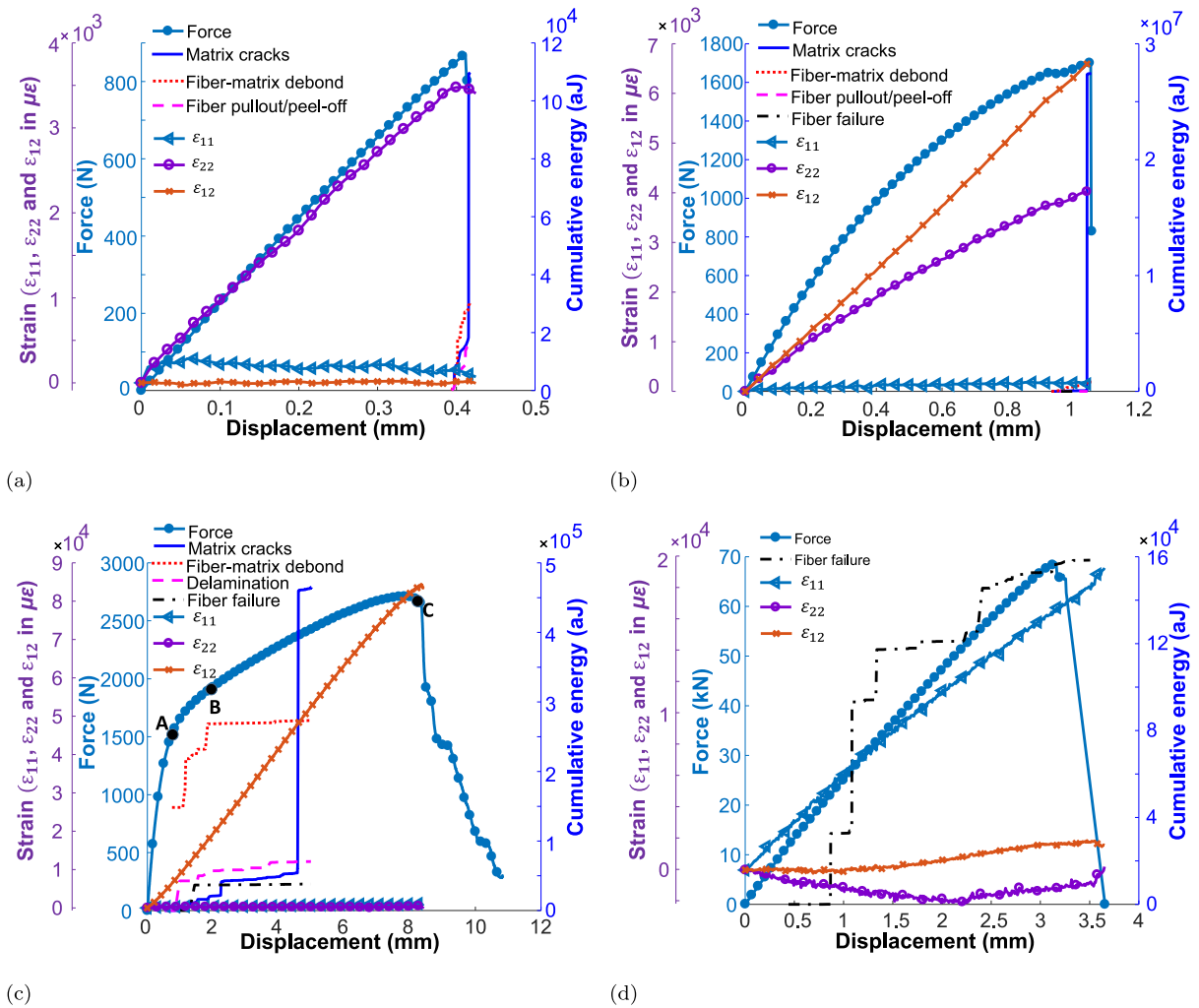
Fig. 15. Variation of strain components and cumulative energy of different damage modes along with the applied load. (a) UD90 specimen (b) UD45 specimen (c) Q±45 specimen (d) UD0 specimen.

crack path of delamination propagation [73]. Fig. 16(b) shows the cumulative energy of different failures for the ENF specimen. After reaching the peak load, the cumulative energy suddenly increases, which is high for matrix damage and delamination failure. The delamination propagation is rapid, and there is a sudden load drop after the delamination initiation at the peak load. This is due to the unstable crack propagation in mode-II delamination [77]. The variation of cumulative energy of different failures for MMB specimen is shown in Fig. 16(c). The failure is governed by both inter-laminar tensile and shear stresses in the MMB specimen. As the failure is governed by mode-I and mode-II delamination, the damage modes of DCB and ENF are observed in the MMB specimen. The cumulative energy for delamination failure increases with a load drop and remains constant when the load increases, which shows that the delamination propagation leads to a sudden load drop. But, for matrix damage, the cumulative energy increases continuously with the load due to mode-I loading. Thus, the damage modes due to mode-I and mode-II loading are differentiated using the AE results.

This section gives the magnitude of failure strains for different damage modes in the laminates. Also, the cumulative energy of different failure modes gives an in-depth understanding of the sequence of damages and their failure mechanism in the laminates. Thus, the study using combined AE and DIC yields information about the damage modes in the laminates, which can be used as input for developing physics-based progressive damage models for composite laminates.

8. Conclusion

This work employs combined AE and DIC techniques to understand and characterize intra/inter-laminar failure mechanisms in CFRP laminate. Experiments are carried out on CFRP laminates under in-plane and out-of-plane loads to comprehend different
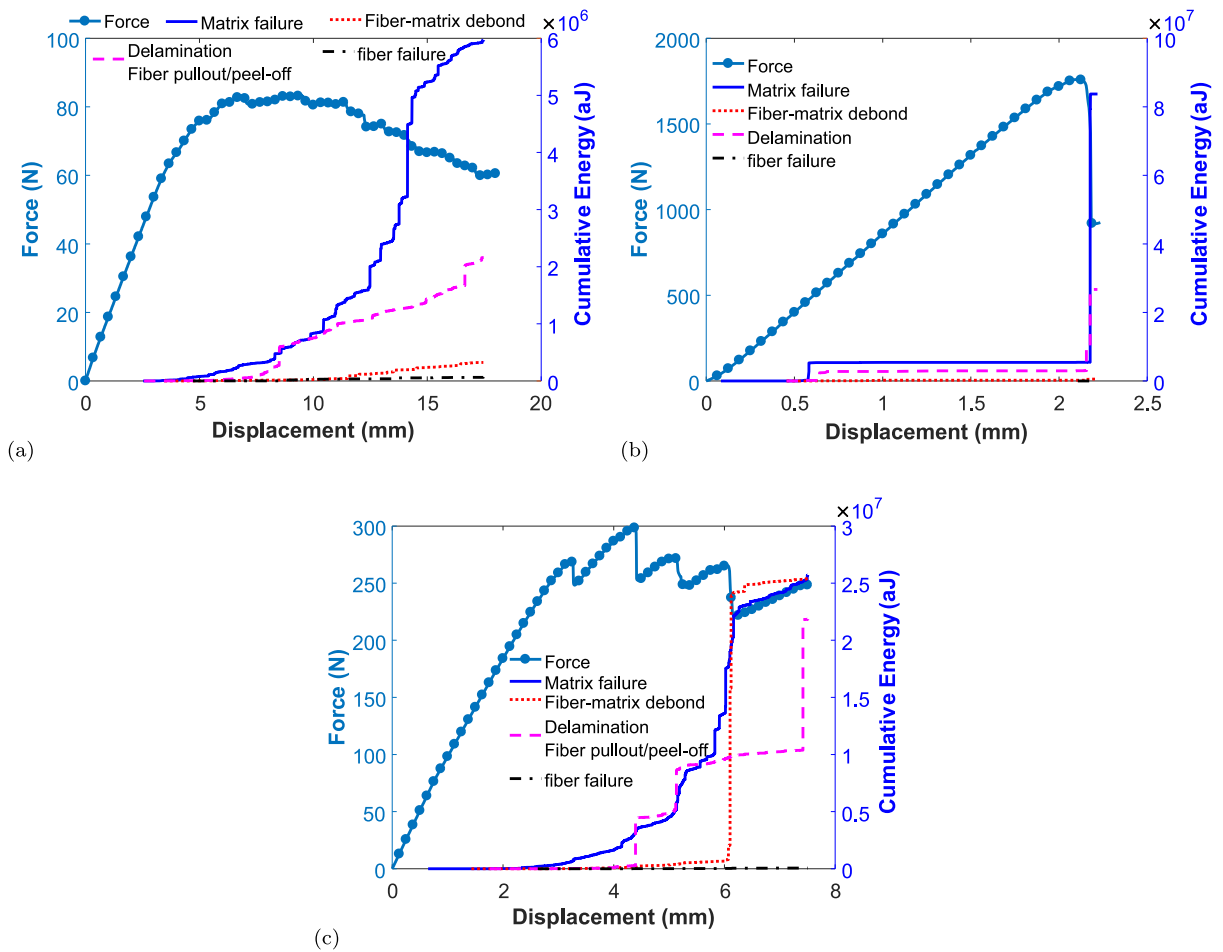
Fig. 16. Variation of cumulative energy for different damages with respect to applied load. (a) DCB specimen (b) ENF specimen (c) MMB specimen.

damage modes and their sequence of occurrence based on AE and DIC observations. An unsupervised k-means clustering technique is employed to classify the AE signals and resulted in three major clusters of data. Further, displacement and strain fields on the surface of the specimen and fractography studies are used to identify the damage modes and their sequence of occurrence in all specimens and assign damage modes to the clusters. Based on the AE results, it is observed that the matrix damage has a low-frequency range (58–175 kHz), whereas fiber fracture has a high-frequency range (> 600 kHz). The fiber–matrix debond (175–400 kHz) and delamination (400–600 kHz) frequency ranges fall between matrix and fiber damages. The frequency range for the delamination and fiber pullout/peel-off is similar (400–600 kHz), but the amplitude range for these two failures is different. Failure strains for different damage modes are evaluated using DIC. Thus the study using AE, DIC, and fractography results lead to a proper understanding of damage modes and failure mechanisms which will help in the development of physics-based progressive damage models and structural health monitoring applications.

CRediT authorship contribution statement

Lala Bahadur Andraju: Writing – original draft, Visualization, Validation, Software, Methodology, Investigation, Formal analysis, Data curation, Conceptualization. **Gangadharan Raju:** Writing – review & editing, Supervision, Resources, Project administration, Methodology, Investigation, Funding acquisition, Conceptualization.

Declaration of competing interest

The authors declare that they have no known competing financial interests or personal relationships that could have appeared to influence the work reported in this paper.
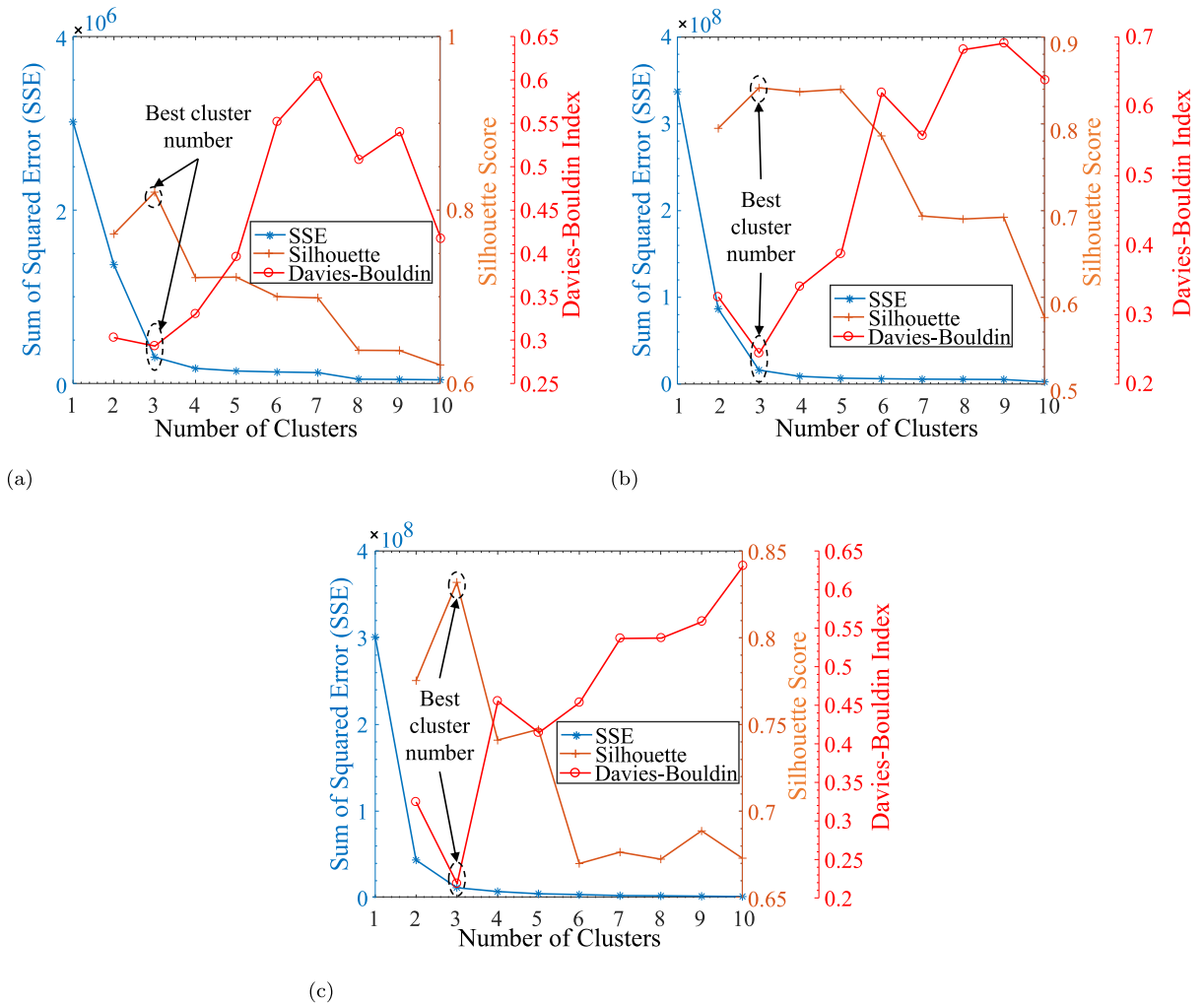
Fig. 17. Optimum number of clusters for composite specimens subjected to tensile loading evaluated using different indices. (a) UD45 (b) Q±45 (c) UD0.
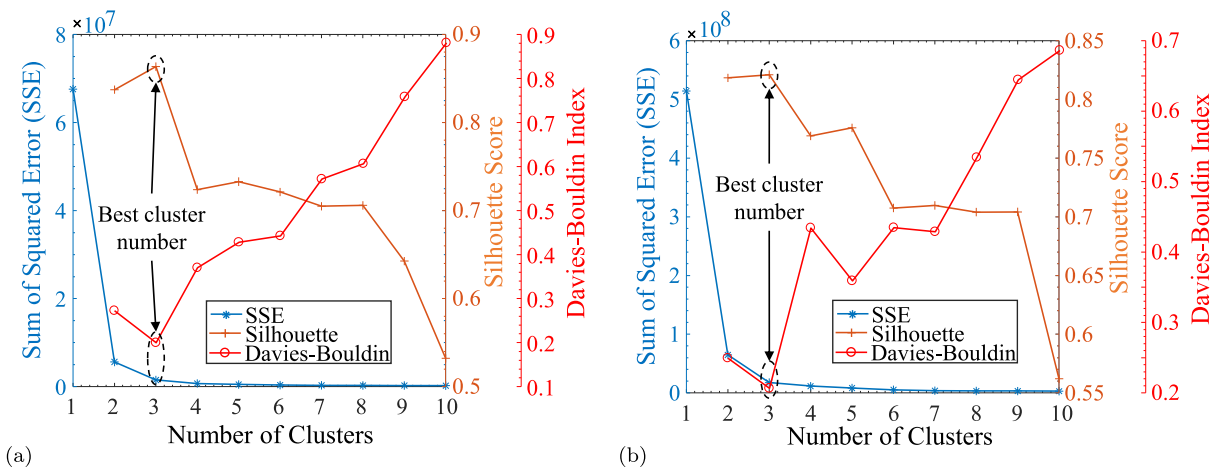

Fig. 18. Optimum number of clusters for the standard specimens used to characterize delamination failure. (a) ENF (b) MMB.

Data availability

Data will be made available on request.

Appendix A

Figs. 17 and 18 show the SSE, Silhouette score, and Davies–Bouldin index variation with the number of clusters for UD45, Q±45, UD0, ENF and MMB specimens.

References

[1] Hamstad MA. A review: acoustic emission, a tool for composite-materials studies. Exp Mech 1986;26(1):7–13.
[2] De Rosa IM, Santulli C, Sarasini F. Acoustic emission for monitoring the mechanical behaviour of natural fibre composites: A literature review. Composites A 2009;40(9):1456–69.
[3] Saeedifar M, Zarouchas D. Damage characterization of laminated composites using acoustic emission: A review. Composites B 2020;195:108039.
[4] Czigany T, Pölöskei K, Karger-Kocsis J. Fracture and failure behavior of basalt fiber mat-reinforced vinylester/epoxy hybrid resins as a function of resin composition and fiber surface treatment. J Mater Sci 2005;40(21):5609–18.
[5] Romhány G, Czigány T, Karger-Kocsis J. Determination of J–R curves of thermoplastic starch composites containing crossed quasi-unidirectional flax fiber reinforcement. Compos Sci Technol 2006;66(16):3179–87.
[6] Grigg S, Pullin R, Featherston C. Acoustic emission source location in complex aircraft structures using three closely spaced sensors. Mech Syst Signal Process 2022;164:108256.
[7] Gangadharan R, Prasanna G, Bhat M, Murthy C, Gopalakrishnan S. Acoustic emission source location in composite structure by voronoi construction using geodesic curve evolution. J Acoust Soc Am 2009;126(5):2324–30.
[8] Kolanu NR, Raju G, Ramji M. Experimental and numerical studies on the buckling and post-buckling behavior of single blade-stiffened CFRP panels. Compos Struct 2018;196:135–54.
[9] Peters WH, Ranson WF. Digital imaging techniques in experimental stress analysis. Opt Eng 1982;21(3):427–31. http://dx.doi.org/10.1117/12.7972925.
[10] Barile C, Casavola C, Pappalettera G, Kannan VP. Application of different acoustic emission descriptors in damage assessment of fiber reinforced plastics: A comprehensive review. Eng Fract Mech 2020;235:107083.
[11] Liu P, Chu J, Liu Y, Zheng J. A study on the failure mechanisms of carbon fiber/epoxy composite laminates using acoustic emission. Mater Des 2012;37:228–35.
[12] Heidary H, Ahmadi M, Rahimi A, Minak G. Wavelet-based acoustic emission characterization of residual strength of drilled composite materials. J Compos Mater 2013;47(23):2897–908.
[13] Huang C, Ju S, He M, Zheng Q, He Y, Xiao J, et al. Identification of failure modes of composite thin-ply laminates containing circular hole under tension by acoustic emission signals. Compos Struct 2018;206:70–9.
[14] Özaslan E, Yetgin A, Acar B, Güler MA. Damage mode identification of open hole composite laminates based on acoustic emission and digital image correlation methods. Compos Struct 2021;274:114299.
[15] Sayar H, Azadi M, Ghasemi-Ghalebahman A, Jafari SM. Clustering effect on damage mechanisms in open-hole laminated carbon/epoxy composite under constant tensile loading rate, using acoustic emission. Compos Struct 2018;204:1–11.
[16] Chelliah SK, Parameswaran P, Ramasamy S, Vellayaraj A, Subramanian S. Optimization of acoustic emission parameters to discriminate failure modes in glass–epoxy composite laminates using pattern recognition. Struct Health Monit 2019;18(4):1253–67.
[17] Jefferson Andrew J, Arumugam V. Effect of patch hybridization on the compression behavior of patch repaired glass/epoxy composite laminates using acoustic emission monitoring. Polym Compos 2018;39(6):1922–35.
[18] Byrne C, Green RE. Acoustic emission monitoring of thick composite laminates under compressive loads. In: Nondestructive characterization of materials VI. Springer; 1994, p. 191–8.
[19] Jayababu A, Arumugam V, Rajesh B, Suresh Kumar C. Investigation of indentation damage resistance on normal and inclined plane of glass/epoxy composite laminates using acoustic emission monitoring. J Compos Mater 2020;54(21):2953–64.
[20] Saeedifar M, Najafabadi MA, Zarouchas D, Toudeshky HH, Jalalvand M. Clustering of interlaminar and intralaminar damages in laminated composites under indentation loading using acoustic emission. Composites B 2018;144:206–19.
[21] Andraju LB, Raju G. Continuum and cohesive zone damage models to study intra/inter-laminar failure of curved composite laminates under four-point bending. Compos Struct 2020;253:112768.
[22] Andraju LB, Ramji M, Raju G. Snap-buckling and failure studies on CFRP laminate with an embedded circular delamination under flexural loading. Composites B 2021;214:108739.
[23] Manterola J, Aguirre M, Zurbitu J, Renart J, Turon A, Urresti I. Using acoustic emissions (AE) to monitor mode I crack growth in bonded joints. Eng Fract Mech 2020;224:106778.
[24] Barile C, Casavola C, Pappalettera G, Kannan VP. Laplacian score and K-means data clustering for damage characterization of adhesively bonded CFRP composites by means of acoustic emission technique. Appl Acoust 2022;185:108425.
[25] Giordano M, Calabro A, Esposito C, D'amore A, Nicolais L. An acoustic-emission characterization of the failure modes in polymer-composite materials. Compos Sci Technol 1998;58(12):1923–8.
[26] Huguet S, Godin N, Gaertner R, Salmon L, Villard yD. Use of acoustic emission to identify damage modes in glass fibre reinforced polyester. Compos Sci Technol 2002;62(10–11):1433–44.
[27] Ech-Choudany Y, Assarar M, Scida D, Morain-Nicolier F, Bellach B. Unsupervised clustering for building a learning database of acoustic emission signals to identify damage mechanisms in unidirectional laminates. Appl Acoust 2017;123:123–32.
[28] Barile C, Casavola C, Pappalettera G, Vimalathithan PK. Damage characterization in composite materials using acoustic emission signal-based and parameter-based data. Composites B 2019;178:107469.
[29] Barile C, Casavola C, Pappalettera G. Acoustic emission waveform analysis in CFRP under mode I test. Eng Fract Mech 2019;210:408–13.

[30] Barile C, Casavola C, Pappalettera G, Paramsamy Kannan V. Damage assessment of carbon fibre reinforced plastic using acoustic emission technique: Experimental and numerical approach. Struct Health Monit 2021;20(3):1090–101.

[31] Nazmdar Shahri M, Yousefi J, Fotouhi M, Ahmadi Najfabadi M. Damage evaluation of composite materials using acoustic emission features and Hilbert transform. J Compos Mater 2016;50(14):1897–907.

[32] Silversides I, Maslouhi A, LaPlante G. Acoustic emission monitoring of interlaminar delamination onset in carbon fibre composites. Struct Health Monit 2013;12(2):126–40.

[33] Fotouhi M, Ahmadi Najafabadi M. Investigation of the mixed-mode delamination in polymer-matrix composites using acoustic emission technique. J Reinf Plast Compos 2014;33(19):1767–82.

[34] Mohammadi R, Saeedifar M, Toudeshky HH, Najafabadi MA, Fotouhi M. Prediction of delamination growth in carbon/epoxy composites using a novel acoustic emission-based approach. J Reinf Plast Compos 2015;34(11):868–78.

[35] Shateri M, Ghaib M, Svecova D, Thomson D. On acoustic emission for damage detection and failure prediction in fiber reinforced polymer rods using pattern recognition analysis. Smart Mater Struct 2017;26(6):065023.

[36] De Groot PJ, Wijnen PA, Janssen RB. Real-time frequency determination of acoustic emission for different fracture mechanisms in carbon/epoxy composites. Compos Sci Technol 1995;55(4):405–12.

[37] Gutkin R, Green C, Vangrattanachai S, Pinho S, Robinson P, Curtis P. On acoustic emission for failure investigation in CFRP: Pattern recognition and peak frequency analyses. Mech Syst Signal Process 2011;25(4):1393–407.

[38] Li L, Lomov SV, Yan X, Carvelli V. Cluster analysis of acoustic emission signals for 2D and 3D woven glass/epoxy composites. Compos Struct 2014;116:286–99.

[39] Johnson M, Gudmundson P. Broad-band transient recording and characterization of acoustic emission events in composite laminates. Compos Sci Technol 2000;60(15):2803–18.

[40] Zhou W, Zhao Wz, Zhang Yn, Ding Zj. Cluster analysis of acoustic emission signals and deformation measurement for delaminated glass fiber epoxy composites. Compos Struct 2018;195:349–58.

[41] Mi Y, Zhu C, Li X, Wu D. Acoustic emission study of effect of fiber weaving on properties of fiber-resin composite materials. Compos Struct 2020;237:111906.

[42] Mohammadi R, Najafabadi MA, Saeedifar M, Yousefi J, Minak G. Correlation of acoustic emission with finite element predicted damages in open-hole tensile laminated composites. Composites B 2017;108:427–35.

[43] Li L, Lomov SV, Yan X. Correlation of acoustic emission with optically observed damage in a glass/epoxy woven laminate under tensile loading. Compos Struct 2015;123:45–53.

[44] Barile C, Casavola C, Pappalettera G, Kannan VP. Interpreting the Lempel–Ziv complexity of acoustic emission signals for identifying damage modes in composite materials. Struct Health Monit 2022. http://dx.doi.org/10.1177/14759217221112831.

[45] Lempel A, Ziv J. On the complexity of finite sequences. IEEE Trans Inform Theory 1976;22(1):75–81.

[46] He X, Cai D, Niyogi P. Laplacian score for feature selection. Adv Neural Inf Process Syst 2005;18(2005).

[47] Cai D, Zhang C, He X. Unsupervised feature selection for multi-cluster data. In: Proceedings of the 16th ACM SIGKDD international conference on knowledge discovery and data mining. 2010, p. 333–42.

[48] Xu D, Liu P, Li J, Chen Z. Damage mode identification of adhesive composite joints under hygrothermal environment using acoustic emission and machine learning. Compos Struct 2019;211:351–63.

[49] Godin N, Huguet S, Gaertner R, Salmon L. Clustering of acoustic emission signals collected during tensile tests on unidirectional glass/polyester composite using supervised and unsupervised classifiers. Ndt E Int 2004;37(4):253–64.

[50] Sause MG, Schmitt S, Kalafat S. Failure load prediction for fiber-reinforced composites based on acoustic emission. Compos Sci Technol 2018;164:24–33.

[51] McCrory JP, Al-Jumaili SK, Crivelli D, Pearson MR, Eaton MJ, Featherston CA, et al. Damage classification in carbon fibre composites using acoustic emission: A comparison of three techniques. Composites B 2015;68:424–30.

[52] Bhat C, Bhat M, Murthy C. Acoustic emission characterization of failure modes in composites with ANN. Compos Struct 2003;61(3):213–20.

[53] Barile C, Casavola C, Pappalettera G, Kannan VP. Damage monitoring of carbon fibre reinforced polymer composites using acoustic emission technique and deep learning. Compos Struct 2022;292:115629.

[54] Rousseeuw PJ. Silhouettes: a graphical aid to the interpretation and validation of cluster analysis. J Comput Appl Math 1987;20:53–65.

[55] Caliński T, Harabasz J. A dendrite method for cluster analysis. Comm Statist Theory Methods 1974;3(1):1–27.

[56] Davies DL, Bouldin DW. A cluster separation measure. IEEE Trans Pattern Anal Mach Intell 1979;PAMI-1(2):224–7. http://dx.doi.org/10.1109/TPAMI. 1979.4766909.

[57] Vesanto J, Alhoniemi E. Clustering of the self-organizing map. IEEE Trans Neural Netw 2000;11(3):586–600.

[58] Liu P, Xu D, Li J, Chen Z, Wang S, Leng J, et al. Damage mode identification of composite wind turbine blade under accelerated fatigue loads using acoustic emission and machine learning. Struct Health Monit 2020;19(4):1092–103.

[59] Maillet E, Godin N, R'Mili M, Reynaud P, Fantozzi G, Lamon J. Damage monitoring and identification in SiC/SiC minicomposites using combined acousto-ultrasonics and acoustic emission. Composites A 2014;57:8–15.

[60] Andrew JJ, Arumugam V, Bull D, Dhakal HN. Residual strength and damage characterization of repaired glass/epoxy composite laminates using AE and DIC. Compos Struct 2016;152:124–39.

[61] Han W, Hu K, Shi Q, Zhu F. Damage evolution analysis of open-hole tensile laminated composites using a progress damage model verified by AE and DIC. Compos Struct 2020;247:112452.

[62] Habibi M, Laperrière L. Digital image correlation and acoustic emission for damage analysis during tensile loading of open-hole flax laminates. Eng Fract Mech 2020;228:106921.

[63] Munoz V, Valès B, Perrin M, Pastor M-L, Welemane H, Cantarel A, et al. Damage detection in CFRP by coupling acoustic emission and infrared thermography. Composites B 2016;85:68–75.

[64] ASTM-D3039. Standard test method for tensile properties of polymer matrix composite materials. West Conshohocken, PA: ASTM International; 2017, 2017 www.astm.org.

[65] ASTM-D5528-13. Standard test method for mode I interlaminar fracture toughness of unidirectional fiber-reinforced polymer matrix composites. West Conshohocken, PA: ASTM International; 2016, 2016 www.astm.org.

[66] ASTM-D7905/D7905M-19e1. Standard test method for determination of the mode II interlaminar fracture toughness of unidirectional fiber-reinforced polymer matrix composites. West Conshohocken, PA: ASTM International; 2019, 2019 www.astm.org.

[67] ASTM-D6671/D6671M-19. Standard test method for mixed mode I-Mode II interlaminar fracture toughness of unidirectional fiber reinforced polymer matrix composites. West Conshohocken, PA: ASTM International; 2019, 2019, www.astm.org.

[68] Caminero MA, Lopez-Pedrosa M, Pinna C, Soutis C. Damage monitoring and analysis of composite laminates with an open hole and adhesively bonded repairs using digital image correlation. Composites B 2013;53:76–91.

[69] Hartigan JA, Wong MA. Algorithm AS 136: A k-means clustering algorithm. J R Stat Soc Ser C (Appl Stat) 1979;28(1):100–8.

[70] Fotouhi M, Heidary H, Ahmadi M, Pashmforoush F. Characterization of composite materials damage under quasi-static three-point bending test using wavelet and fuzzy C-means clustering. J Compos Mater 2012;46(15):1795–808.

[71] Pashmforoush F, Khamedi R, Fotouhi M, Hajikhani M, Ahmadi M. Damage classification of sandwich composites using acoustic emission technique and k-means genetic algorithm. J Nondestruct Eval 2014;33(4):481–92.

[72] Pashmforoush F, Fotouhi M, Ahmadi M. Damage characterization of glass/epoxy composite under three-point bending test using acoustic emission technique. J Mater Eng Perform 2012;21(7):1380–90.

[73] Johnson WS, Mangalgiri P. Investigation of fiber bridging in double cantilever beam specimens. J Composit Technol Res 1987;9(1):10–3.

[74] Kaute DA, Shercliff HR, Ashby MF. Delamination, fibre bridging and toughness of ceramic matrix composites. Acta Metall Et Mater 1993;41(7):1959–70.

[75] Daneshjoo Z, Shokrieh M, Fakoor M. A micromechanical model for prediction of mixed mode I/II delamination of laminated composites considering fiber bridging effects. Theor Appl Fract Mech 2018;94:46–56.

[76] ASTM-D3518/D3518M-13. Standard test method for in-plane shear response of polymer matrix composite materials by tensile test of a ±45° laminate. West Conshohocken, PA: ASTM International; 2018, 2018, www.astm.org.

[77] Benzeggagh ML, Kenane M. Measurement of mixed-mode delamination fracture toughness of unidirectional glass/epoxy composites with mixed-mode bending apparatus. Compos Sci Technol 1996;56(4):439–49.